

UC Irvine

UC Irvine Electronic Theses and Dissertations

Title

Investigating Oxygen Content in Porous Transport Layers of PEM Electrolyzers with Operando X-Ray Computed Tomography and Machine Learning

Permalink

<https://escholarship.org/uc/item/1322c5d7>

Author

O'Brien, Maeve

Publication Date

2020

Peer reviewed|Thesis/dissertation

University of California, Irvine

Investigating Oxygen Content in Porous Transport Layers of PEM Electrolyzers with Operando
X-Ray Computed Tomography and Machine Learning

THESIS

submitted in partial fulfillment for the degree of

MASTER OF SCIENCE

in Materials Science and Engineering

by

Maeve O'Brien

Thesis Committee:
Assistant Professor Iryna Zenyuk, Chair
Professor Plamen Atanosov
Assistant Professor Shane Ardo

2020

Dedication

In loving memory of my grandfather, Benjamin Patrick Oseguera, who passed on 5/19/2020. He was a marine, a mechanic, a sheriff, and a great grandfather to me and my little brother for twenty-four years. May he rest in peace.

Table of Contents

	Page
TABLE OF FIGURES	V
ACKNOWLEDGEMENTS	VII
ABSTRACT OF THE THESIS	VIII
CHAPTER 1-INTRODUCTION TO ELECTROLYZERS.....	1
1.1. INTRODUCTION	1
1.2. BASIC OPERATION OF A PEM ELECTROLYZER	3
1.3. X-RAY COMPUTED TOMOGRAPHY, RADIOGRAPHY AND IMAGING	7
1.4. MACHINE LEARNING FOR IMAGE PROCESSING.....	9
1.5 CURRENT CHALLENGES AND OXYGEN CONTENT IN PTLs	9
1.6- PAST WORK ON IMAGING ELECTROLYZERS AND THIS WORK'S CONTRIBUTION.....	13
CHAPTER 2- EXPERIMENTAL PROCEDURE AND MATERIALS	14
2.1- X-RAY COMPUTED TOMOGRAPHY AND RADIOGRAPHY	14
2.2 – MATERIALS	15
2.3- <i>OPERANDO</i> CELL DESIGN.....	17
2.4 – ELECTROCHEMICAL CHARACTERIZATION AND OPERATION	18
2.5- IMAGE PROCESSING AND VISUALIZATION	19

2.6- MACHINE LEARNING WITH WEKA ALGORITHM IN IMAGEJ	20
CHAPTER 3. DATA INTERPRETATION AND ADDITIONAL DETAILS.....	22
3.1-CHAPTER INTRODUCTION.....	22
3.2- A GUIDE TO INTERPRETING TOMOGRAPHY DATA	22
3.3- OXYGEN CONTENT MEASUREMENTS AND VISUALIZATION	25
CHAPTER 4- RESULTS.....	27
4.1- CHAPTER INTRODUCTION.....	27
4.2- ELECTROCHEMICAL POLARIZATION AND CHARACTERIZATION	27
4.3- CROSS-SECTIONS OF GREY-SCALE IMAGES OF ELECTROLYZER UNDER VARIED CURRENT DENSITIES AND WATER FLOWRATES	30
CHAPTER 5- CONCLUSIONS	42
REFERENCES.....	45

Table of Figures

Figure 1. A diagram detailing power-to-gas, an approach to avoid energy curtailment. ¹	1
Figure 2. A diagram illustrating the basic operation of a PEM electrolyzer, with the PEM membrane in light yellow, and the cathode catalyst layer in green, and the anode catalyst layer in red.	4
Figure 3. An example polarization curve for a PEM electrolyzer, where the areas of kinetic, ohmic and mass transport losses are noted.	6
Figure 4. The differences between x-ray computed tomography and radiography, including the pros and cons of both techniques ⁹	8
Figure 5. Bubble nucleation and movement captured with a high-speed optical camera with micrometer resolution from a transparent PEM electrolyzer ¹⁶	11
Figure 6. Neutron radiography of the anode and cathode-side PTLs of an operating PEM electrolyzer, done over a range of current densities from 0.1 to 2.5. The color bar measures the water thickness, ranging from 0mm to 3.5mm ¹⁷	12
Figure 7. A disassembled electrolyzer cell, with titanium PTL (middle) wetted from testing, and Teflon gasket exposed.....	16
Figure 8. (A) the fully assembled PEM electrolyzer cell, and (B) the exploded view of the PEM electrolyzer cell, with the GDL, PTL and ionomer (PEM membrane) noted.	17
Figure 9. Examples of images pre(left) and post(right) processing with Weka. Post processing, the image is segmented into areas of oxygen, in red, and areas of either water or fiber which is displayed as green.	22
Figure 10. A 3D representation of a traditional PEM electrolyzer, where the relevant views examined in this study are noted in red. The Ti PTL is in yellow, and the carbon paper GDL is in gray.	24
Figure 11. Labeled cross-sections detailing how to interpret the tomography cross-sections in different points of view. All z-projects, and Weka training were done with x-z plane slices.	25
Figure 12. Polarization(A) and EIS (B) of the cells prior to in-situ x-ray computed tomography.	28
Figure 13. Potential holds during testing, ranging from 1A(a) through 2A(b), for each flow rate.	29
Figure 14. Potential holds during testing, ranging from(A)3A to 4A for each flowrate.	29
Figure 15. X-Y plane view of an electrolyzer at OCV. It is important to note that the PTL, which is a treated Freudenberg GDL, is saturated with water.....	31
Figure 16. X-Y plane view of the PEM electrolyzer during operation, where (A) is 1A 1mlpm, increasing up to (C) of 1A and 3mlpm.	31
Figure 17. X-Y plane view of the PEM electrolyzer in operation, where (A) is 4A 1mlpm, (B) 4A 2mlpm, and (C) 4A 3mlpm.	32
Figure 18. X-Z plane view of the PTL during operation at 1A and 1mlpm, where (A) is a cross-section taken near the land and channel, and (B) is a cross-section taken near the catalyst layer. ³⁴	
Figure 19. X-Z plane view of the PTL during operation at 4A and 3mlpm, where (a) is a cross-section taken near the land and channel, and (b) is a cross-section taken near the catalyst layer. ³⁴	

Figure 20. Oxygen content as a function of through-thickness PTL location for constant current densities and varied flowrates. The location of the channel is noted with the orange box and label..... 36

Figure 21. Oxygen content figures comparing the through-thickness for varied current and constant flowrates. The location of the channel is noted with the orange box and label..... 37

Figure 22. Oxygen content measurements along the length of the PEM electrolyzer, where (A) compared the same current density at different flowrates and (B) compared different current densities at the same flowrate. 38

Figure 23. (A) through (C) are Z-projects of the x-z plane of the PTL at different current densities and the same flowrate, in the top row. (D) through (F) are z-projects of the catalyst layer..... 40

Figure 24. A schematic representation of possible preferential pathways represented by the funnel through the PTL. The area that was used to generate the oxygen content figures is highlighted by the dashed red box. 42

Acknowledgements

To my mother, father, and little brother- thank you for all your support throughout my academic career. There are no words to describe how thankful I am, except I love and appreciate you all.

To my advisor, Dr. Iryna Zenyuk, I want to offer a heartfelt thanks for her boundless patience, understanding, and mentorship through my time at UC Irvine. I got the chance to do work and meet people I never would have had I not joined the Zenyuk group and for that I will always be grateful.

To my lab mates, Devashish and Ying- thank you for your guidance and companionship during long hours either during preparation for beamtime, at beamtime, or in the office. I will look back on our times together fondly. Also, Devashish is responsible for the lovely diagram in Figure 8, and for that I am very thankful.

To Katie, Chloe, Sasha, Adam and Mark- thank you for all our lunches we spent together, and all the times I laughed so hard I cried a little during them.

Abstract of the Thesis

Investigating Oxygen Content in Porous Transport Layers of PEM Electrolyzers with Operando

X-Ray Computed Tomography and Machine Learning

THESIS

submitted in partial fulfillment for the degree of

MASTER OF SCIENCE

in Materials Science and Engineering

by

Maeve O'Brien

University of California, Irvine

Assistant Professor Iryna Zenyuk, Chair

Hydrogen gas is a good candidate to replace traditional, carbon-based energy carriers; it is easily transported, and many vehicles already utilize hydrogen-based fuel cells to power locomotion. To produce hydrogen gas, water electrolysis is the go-to electrochemical process. Although water electrolysis is a well-understood process, the morphological and transport processes inherent to a proton exchange membrane (PEM) electrolyzer and how these affect the efficiency of water electrolysis in a PEM electrolyzer are still relatively unexplored. In order to probe these processes in-situ, x-ray computed tomography and radiography were performed on catalyst coated membranes (CCM) of a model electrolyzer at different flowrates and current densities to determine how these different operating conditions alter the oxygen production, slug or bubble formation, and dwell time in the porous transport layer (PTL). X-ray computed tomography was utilized to create 3D images, and radiography was utilized to visualize transient

oxygen production and dwell time in-situ. Machine learning was used to quantify the oxygen content in the model electrolyzer, as well as any pathways or patterns the oxygen took as it exited the electrolyzer through the PTL. From these results there was a direct observation of oxygen taking preferential pathways through the PTL regardless of the flow rate or current density, and at higher current densities more oxygen became trapped beneath the land. This is the first time this phenomenon has been directly observed with x-ray computed tomography and is in good agreement with recent neutron radiography experiments using Ti PTLs.

Chapter 1-Introduction to Electrolyzers.

1.1. Introduction

Bolstered by the issue of climate change, a shrinking global fossil fuel supply and the overall increase of the global population many countries are making the switch from non-renewable to renewable energy sources in order to reduce their reliance on non-renewable energy sources. However, as the percentage of renewable versus non-renewable energy sources in the power supply shifts to favor renewable energy sources, the issue of curtailment becomes more and more pressing.¹ Curtailment is essentially the deactivating of renewable energy sources, for example, wind turbines or solar cells, when the energy generated exceeds the instantaneous demand for energy at that time; this leads to the excess energy going to waste.^{2,3} Curtailment occurs during the daytime, as the power being generated exceeds the instantaneous consumer demand on the power grid. For example, as much as 150,000 MWh of energy was curtailed in March of 2020 in California alone.³

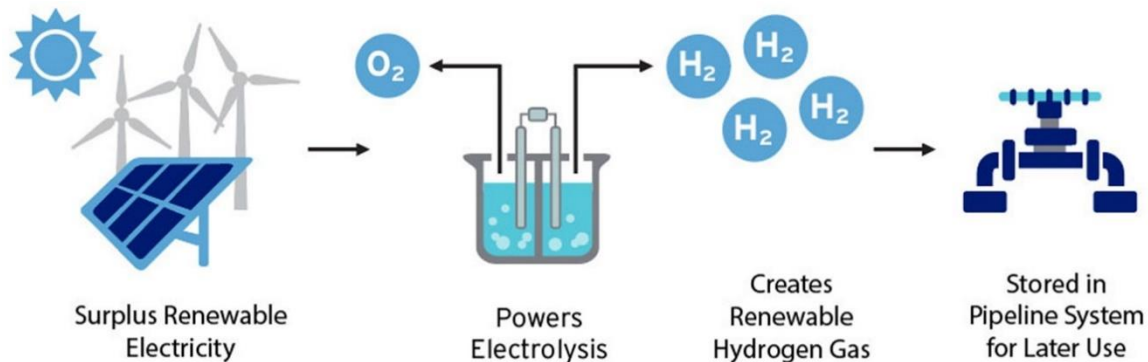


Figure 1. A diagram detailing power-to-gas, an approach to avoid energy curtailment.¹

We need to capture this curtailed energy and store it for later use. A potential solution is in storing the excess energy in the form of hydrogen. As shown by Figure 1, the excess energy generated by renewable energy sources (wind and solar) can be used to power a water electrolyzer stack.^{4,5} Water electrolysis is an already well-established and well-understood

process, that utilizes electricity in order to convert water into oxygen and hydrogen. The product of interest from water electrolysis is hydrogen as it is fuel and can be easily stored as compressed gas, transported via natural gas pipelines, and then later combusted as a fuel source or converted back to electricity in PEM fuel cells. Hydrogen has a high net mass energy density of 120 MJ/kg and therefore is competitive as a fuel.⁶

Although water electrolysis itself is a well-established method for producing hydrogen, there remains several factors that can be optimized to develop an electrolyzer stack that both minimizes the cost to produce as well as maximizes its efficiency in converting water to hydrogen and oxygen. In order to reduce the cost of producing electrolyzer stacks, both industry and academic research groups have made great strides in reducing the electrocatalyst loading in the electrolyzer stacks; typical electrocatalysts are Ir or Pt, both very costly and account for approximately 30-35%⁶ of the overall cost of the electrolyzer stack. Beyond this, recent advances have allowed for cheaper production of bipolar plates and porous transport layers- both have been traditionally made from titanium-since this metal does not corrode at the high potentials required for anode operation- and required costly manufacturing techniques.

With these reductions in cost, producing electrolyzer stacks on a scale necessary to support a modern power grid is within reach.⁷ However, there are still important processes that require further investigation before such a step can be taken. While water electrolysis is a well-understood chemical process, the minutiae of how these recent advances alter the two-phase flow phenomena in an electrolyzer stack need to be investigated further. Throughout the operation of an electrolyzer stack, water flows in via the anode and transports through the porous transport layer (PTL), to each catalyst layer. Once in contact with the catalyst, the water is split into protons, electrons and oxygen gas; although it should be noted that some of the by-product

oxygen exists either as dissolved oxygen or bubbles. These oxygen bubbles can prove to be problematic during the operation of an electrolyzer stack, as it can block water from reacting with the electrocatalyst, thus decreasing the overall electrolyzer efficiency.

1.2. Basic Operation of a PEM Electrolyzer

An electrolyzer is an electrochemical energy-conversion device that uses electricity and water to generate hydrogen and oxygen gas. The thermodynamic potential of an H₂-O₂ couple is 1.23V. When a potential is applied above 1.23V, an oxygen evolution reaction (OER) occurs on the anode and a hydrogen evolution reaction (HER)⁸, on the cathode. The produced hydrogen gas has a mass energy density of 120 MJ/kg, whereas gasoline has a mass energy density of 44 MJ/kg; this difference in mass energy density values is what makes hydrogen an attractive alternative fuel, as hydrogen has approximately 2.7 times the amount of energy per kg than liquid gasoline⁶. The electrolyzer cell consists of a porous transport layer (PTL), membrane-electrode assembly (MEA), and gas diffusion layer (GDL). The MEA is in the center of the electrolyzer and consists of a membrane and catalyst layers. The catalyst layers are Ir mixed with Nafion ionomer on the anode, and Pt/C with ionomer on the cathode. A diagram of a PEM electrolyzer is show in Figure 2.

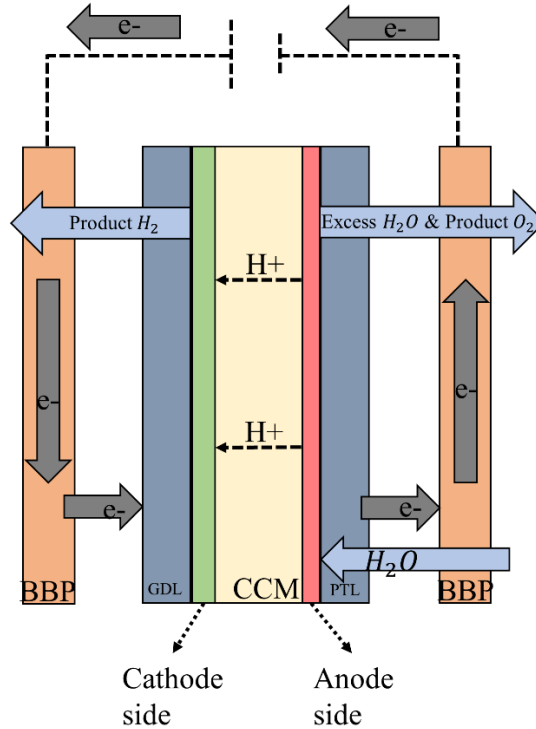
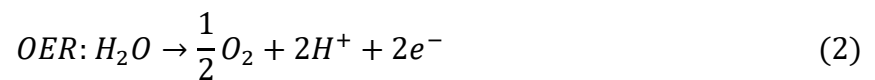
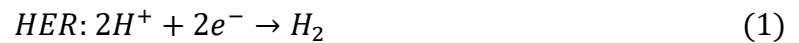


Figure 2. A diagram illustrating the basic operation of a PEM electrolyzer, with the PEM membrane in light yellow, and the cathode catalyst layer in green, and the anode catalyst layer in red.

During operation water is introduced at the anode side of the cell, where it reacts in the catalyst layer, and splits into protons, electrons and oxygen. Protons are transported across the proton exchange membrane (PEM) to the cathode catalyst layer, where the protons combine with incoming electrons in HER. The cathode and anode reactions in a PEM electrolyzer are described respectively as follows:



The net reaction results in hydrogen gas, which then exits the electrolyzer via the GDL on the anode side and can be collected and stored. The efficiency of an electrolyzer can be defined in multiple ways. Faradic efficiency is defined as:

$$\eta_F = \frac{\dot{m}nF}{IM_i} \quad (3)$$

where, \dot{m} is the mass flowrate, I is the total current applied to the cell, n is number of electrons transferred in the reaction and F is the Faraday's constant. The denominator of this equation comes from Faraday's law for the theoretical mass of an electrolysis reaction. If all the electricity is converted into H_2 , then the Faradaic efficiency is 100%. However, inefficiencies exist due to side-reactions that consume electricity but do not produce hydrogen, insufficient contact between the catalyst and the PTL or GDL, or catalyst being blocked by unremoved oxygen bubbles.

Overall energy efficiency of the electrolyzer can be described as:

$$\eta_{energy} = \eta_F \times \frac{U}{V_{cell}} \quad (4)$$

where, η_F is the Faradaic efficiency, U is the thermoneutral potential, and V_{cell} is the applied potential of the cell. Therefore, overall energy efficiency depends on the efficiency of hydrogen production (the Faradaic efficiency) and the efficiency of energy use (the voltage efficiency). An electrolyzer that operates with high energy efficiency will be able to effectively convert electricity to hydrogen at low applied potentials. However, the lower the current densities (and the higher the η_F , the larger the electrolyzer reactor is needed to produce the hydrogen at scale. A compromise is generally achieved between current density, Faradaic and voltage efficiencies when electrolyzers are designed. Another measure of performance for an electrolyzer is its polarization curve, which is shown in Figure 3.

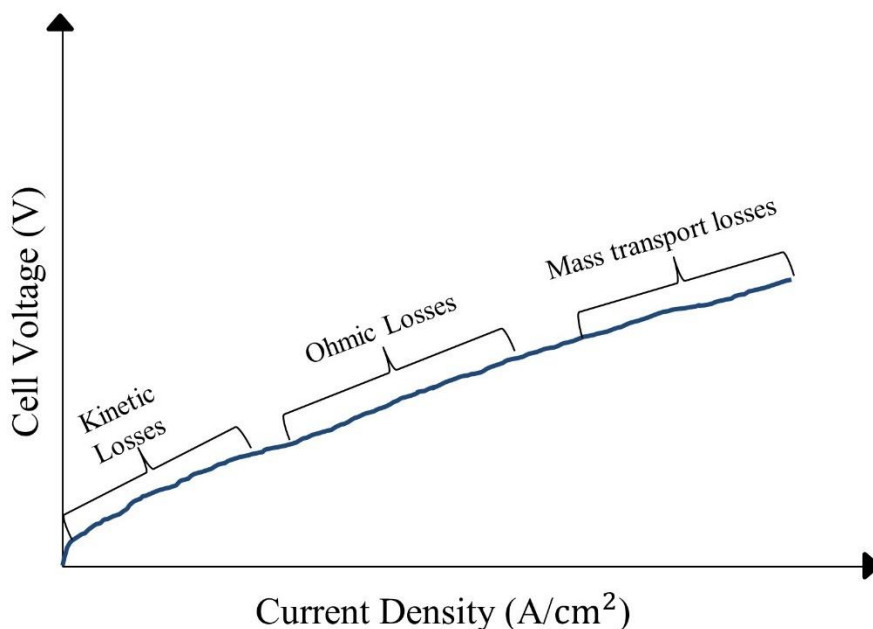


Figure 3. An example polarization curve for a PEM electrolyzer, where the areas of kinetic, ohmic and mass transport losses are noted.

An example of a polarization curve is shown in Figure 3. Polarization curve describes electrolyzer applied potential as a function of current density. The polarization curve consists of kinetic regime where kinetic losses are mainly due to sluggish OER. The Ohmic losses are due to membrane and constant resistances, whereas the mass transport losses are due to issues with oxygen removal from the cell. The kinetic region is closest to the thermodynamic potential, the ohmic region is approximately between 1000 and 1500 mA/cm², and the mass transport region is above 2000 mA/cm². Because water is present in the electrolyzer in a ratio to one water molecule to ½ an O₂ molecule, and is a reactant on the anode, the OER is not reactant limited. But it can be limited by the removal of oxygen from the surface of the catalyst. Generally, the lower the applied potential that results in the same current density the more efficient an electrolyzer is. Voltage efficiency is defined as:

$$\eta_V = \frac{E_{th}^o}{E} \quad (5)$$

where, E_{th}^o is the thermoneutral potential (1.48 V), and E is the operating potential of the cell. For the most voltage efficient operation, the electrolyzer's operating potential needs to be close to the thermoneutral potential, 1.23V. In addition, the polarization curve in Figure 3 can be divided into the kinetic, ohmic and mass-transport regions.

As shown in Figure 2, the PTLs and GDLs should conduct electrons and manage mass transport. Both the PTL and GDL are purposefully designed with voids or pores in order to facilitate transport of the reactants and products to and from the catalyst layers of the MEA, and the solid portions of the PTLs and GDLs allow for the transport of electrons and heat to the bipolar plates (BPPs) to complete the reaction.

1.3. X-Ray Computed Tomography, Radiography and Imaging

X-ray computed tomography was a technique originally intended for use with biological materials and in more recent decades has become ubiquitous in the medical profession as CAT scans. However, x-ray computed tomography has found a second life as a non-destructive technique with non-biological samples. Perhaps most useful is that in-situ experiments can be run in order to better understand how chemical, mechanical, or electrochemical processes can influence the morphology of the sample⁹. Additionally, these in-situ experiments can also be used to study the mass transport efficiency of porous media, which had been the main interest of this study.

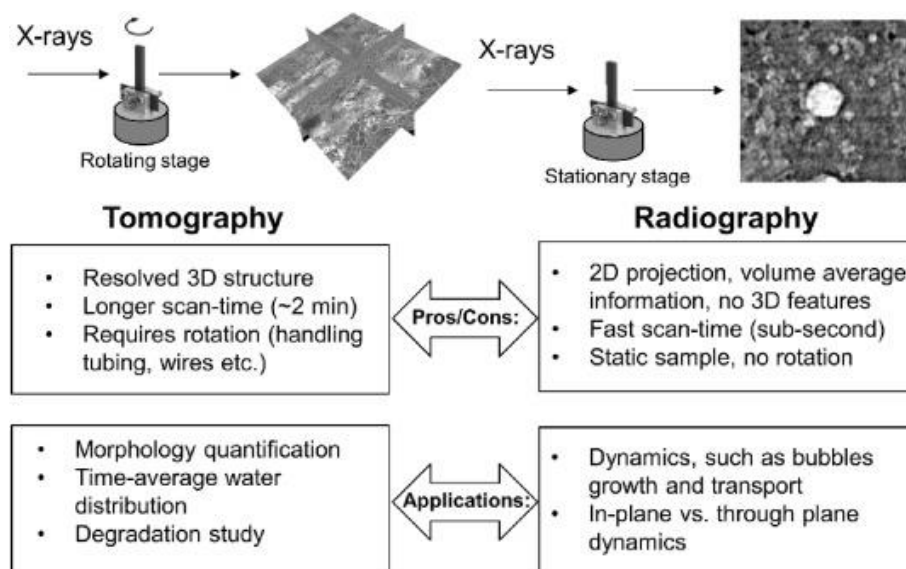


Figure 4. The differences between x-ray computed tomography and radiography, including the pros and cons of both techniques⁹.

X-ray computed tomography generates 3-D data that provides useful morphological and transport information about the sample being analyzed. This 3-D data is captured by rotating the sample on a rotating stage transmitting the sample with x-rays. Once the x-rays pass through the sample, they are captured with detectors opposite from the optics and eventually processed via the connected computer; after being processed, the data is transferred to external harddrives for easier transport from the beamline to UC Irvine for further analysis. The details of the analysis done upon the data collected in discussed in more depth in Chapter 2.

X-ray radiography is 2-D technique, where the X-rays transmit through the sample and are collected with the detector. X-ray radiography form the basis for tomography, as multiple radiographs are collected during X-ray CT scan. The advantage of X-ray radiography is that the information can be captured on ms scale. Radiography is relevant to capture transient phenomenal in electrolyzers, such as oxygen evolution and transport. X-ray CT scans generally still require 3 minutes per scan and thus cannot be used for transient imaging.

1.4. Machine Learning for Image Processing

From fields such as computer science¹⁰, biology¹¹, and social media analytics¹² machine learning has become increasingly useful in recent years for enhancing our understanding of large amounts of data. Machine learning is a subset of artificial intelligence, wherein a program is trained through a smaller subset of data, and through experience learns how to differentiate between different data points as set by the trainer. After each successive training session, the algorithm is updated to reflect what was categorized correctly and what was incorrectly categorized. This updating process is essentially adding negative or positive values associated with the earlier segmentation of the smaller data set, in order to either encourage or discourage the selection of certain data points. This is repeated several times until the accuracy of the algorithm is as close to perfect as possible. Once the accuracy is satisfactory, the algorithm is then applied to the whole data set.¹³ For this project, machine learning was utilized to analyze the amount of oxygen present in the porous transport layers of the electrolyzers at varying flow rates and current densities; more specifics of the algorithm training process can be found in Chapter 2.

1.5 Current Challenges and Oxygen Content in PTLs

Though there have been recent advancements in the field's understanding of PEM electrolyzers, there are still several issues associated with both the overall efficiency as well as the cost.¹⁴ Similarly, to fuel cells, the bulk of an electrolyzer cell's cost is associated with the catalysts. Typically Pt and Ir are used as catalysts in electrolyzers, for the cathode and anode respectively, and while they are some of the best catalysts for HER and OER, they are very expensive and can account for up to 35% of the total electrolyzer cell cost⁶. Another major

source of the cell cost is the porous transport layer (PTL), which is typically produced from titanium. Ti is favored for its durability on the anode side of the electrolyzer, which operates at potentials above 2 V. However, with these PTLs durability comes the cost of the material itself. The combined costs of the catalysts as well as the PTL material makes it difficult for the commercialization of electrolyzers, with the PTL accounting for 17-25% of the total stack cost, and the Ti feedstock powder costing \$35/kg¹⁵.

Some proposed solutions to approach the issue of the efficiency of PEM electrolyzers has been to add a microporous layer (MPL) to the PTL. This approach has been widely utilized in PEM fuel cells, specifically to increase product/reactant removal as well as increase catalyst access, but until recently has not been studied in PEM electrolyzers. Kang et al.¹⁶ studied how the addition of an MPL would alter the operation of a PEM electrolyzer by developing a thin-tunable liquid/gas diffusion layers(TT-LGDLs) and observing their performance in-situ by constructing a transparent PEM electrolyzer and recording the behavior with a high speed camera. Although the TT-LGDLs constructed with a micro particle MPL exhibited improved catalytic activity, they also exhibited increased ohmic resistance in addition to super hydrophobic properties. These results from Kang et al. demonstrate that TT-LDGLs do indeed have a future for use in PEM electrolyzer and have also further probed the nature of oxygen formation by utilizing visual dynamic imaging.

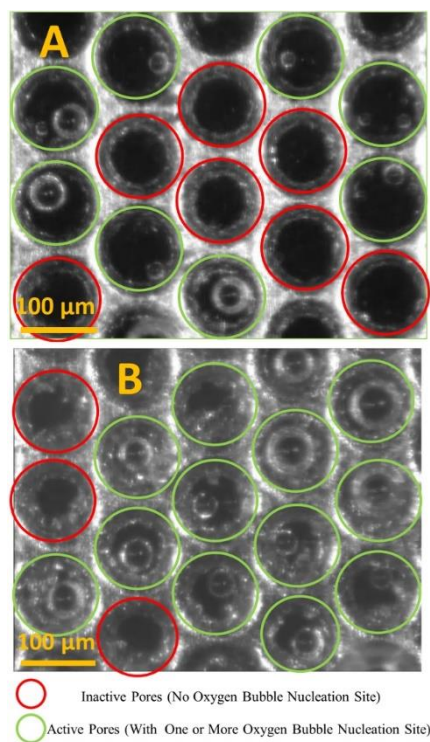


Figure 5. Bubble nucleation and movement captured with a high-speed optical camera with micrometer resolution from a transparent PEM electrolyzer¹⁶.

In a similar vein to Kang et al.'s optical approach, Seweryn et al.¹⁷ utilized neutron imaging to probe the water/gas distribution in the anode side PTL. Neutron imaging, unlike the optical technique utilized by Kang et al, does not require the PEM electrolyzer to be transparent in order to image the water/gas distribution, and it does not require a change in the PTL material. Seweryn et al. observed a pattern in the water/gas distribution in the anode-side PTL that varied very little with both the flowrate of water and the applied current density. However, neutron radiography has a lower temporal and spatial resolution than x-ray imaging, which is a disadvantage when trying to understand gas evolution in the anode-side PTL. Water thickness of approximately 1.5 mm was observed for current density ranging from 0.2 to 2.5A/cm², and oxygen flux is related to current density through Faraday's law, also incorporated in Equation

(3). As shown in Equation 3, there is a direct relationship between the current density and oxygen flux. However, Seweryn et al. did not observe a change in oxygen content at the anode PTL as current density increased from 0.1 to 2.5 A/cm². This result is indicative that oxygen takes the same pathways, regardless of the current density applied. This is unexpected, as intuitively one will expect to have increasing oxygen content in PTL with increase in current density. The limitations of neutron imaging are: 1) neutron imaging has a spatial resolution of approximately 10um or lower, therefore it does not allow spatially resolved oxygen content within the PTL, 2) it is a 2-D technique and does not capture 3-D information and 3) it requires about an hour to collect an image, thus it is slow.

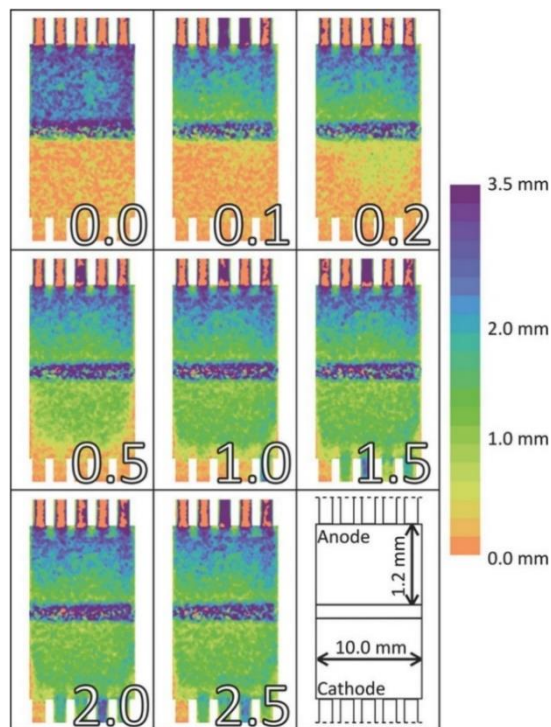


Figure 6. Neutron radiography of the anode and cathode-side PTLs of an operating PEM electrolyzer, done over a range of current densities from 0.1 to 2.5. The color bar measures the water thickness, ranging from 0mm to 3.5mm¹⁷.

Although Kang et al's approach to *in-situ* visualization with an optical high-speed camera was an important advancement in the literature, and Seweryn et al. were able to observe a pattern in the water/gas distribution via neutron imaging, a technique with better temporal and spatial resolution is needed to understand oxygen content and oxygen transport through the PTL. The Zenyuk group turned to *in-situ* x-ray computed tomography and radiography to address this gap in the literature. Specifically, a combination of x-ray computed tomography, radiography and machine learning were utilized in this work in order to gain further insight into how oxygen evolves and exits the PTL of the PEM electrolyzer during operation.

1.6- Past Work on Imaging Electrolyzers and This Work's Contribution

Numerous studies have focused on using imaging techniques to investigate the evolution and transport of oxygen in electrolyzers, ranging from computational studies, optical, neutron or x-ray imaging.¹⁸⁻²¹ Optical microscopy was utilized by Dedigama et al in order to study two-phase flow in an operating electrolyzer²². With a 7000fps camera, as well as a transparent sheet and specific backlighting, they were able to capture anodic two-phase behavior with high temporal accuracy. Neutron imaging has also been utilized to study by Seweryn et al. They were able to observe oxygen residence time in a PTL, specifically titanium, and demonstrated an equilibrium in the two-phase flow in the PTL. Their observations appeared to suggest that the PTL would always be saturated with water, regardless of the current density¹⁷. More recently, Leonard et al. were able to observe oxygen bubble formation and transport with x-ray computed tomography and radiography in an *in-situ* electrolyzer experiment⁹. This work demonstrated that as the current density increased, the residence time of oxygen bubbles decreased; this was

expected, as higher current density would result in more oxygen being formed, and therefore the bubbles would be detached more rapidly.

With the precedent set by Leonard et al, our aim of this project is to investigate both oxygen content in the PTLs and its relation to both electrolyzer current density and water flowrate, as well as understand whether oxygen takes preferential pathways when exiting the PTL. To that end, we set-up a model electrolyzer with a treated carbon fiber material PTL in order to directly observe and quantify both the oxygen content and preferential pathways oxygen could take as it exited PTL. The challenge with Ti PTL is that its X-ray attenuation is much higher than water or oxygen and therefore, it is not possible to distinguish between water and oxygen within the Ti PTL. Using carbon-fiber PTLs and short experimental imaging time we were able to directly observe the steady-state pathways for oxygen transport within the carbon PTL. This is unprecedented as no previous study has seen the pore-scale observation of oxygen content within the PTL with operando techniques.

The thesis is scheduled as following: Chapter 2 describes the experimental condition, Chapter 3 focuses on how to interpret X-ray CT data and provides additional details on data quantification, Chapter 4 focuses on the results and Chapter 5 presents the conclusions of the study and future recommendations.

Chapter 2- Experimental Procedure and Materials

2.1- X-Ray Computed Tomography and Radiography

All x-ray computed tomography and radiography studies were conducted at the Advanced Light Source (ALS), on beamline 8.3.2, at the Lawrence Berkeley National

Laboratory (LBNL). The optics used were as follows: 50um LuAg: Ce scintillator, 5x lenses, a sCMOS PCO Edge camera, and a double multilayer monochromator. The radiographs were collected with 300 ms exposure time and with 1080 number of projections per 180-degree rotation. The resulting images had a voxel resolution of 1.3 um and a horizontal field of view (FOV) of 3.3mm. The beam energy selected was 30 keV. The x-ray computed tomography images required sample rotation, and therefore special care had to be taken so that the water inlet and gas outlets, as well as the thermocouples, did not become tangled; there was a 180-degree rotation. These parameters resulted in a scan time of ~6minutes. In contrast, the radiography scans did not require any rotation, and images were acquired with an exposure time of 100ms.

2.2 – Materials

The catalyst coated membranes (CCMS) used in this experiment were provided by our collaborators (NEL Hydrogen, Wallingford, CT), and consisted of CCMs with catalyst loadings of 3mg/cm² of Pt on the cathode and 3mg/cm³ IrOx on the anode. The PTLs that were used were treated and untreated Freudenberg carbon paper (Fuel Cell Store, College Station, TX) without MPL, for cathode and anode, respectively. Two Freudenberg GDLs with 50 % compression were used to simulate morphology of Ti PTLs. The compressed GDLs should have pore sizes of less than 10 um in diameter, which is what the typical pore sizes for sintered Ti PTLs. The treatment used was applying a piranha solution (HCl) to the desired PTLs in order to make them hydrophilic; this would also allow us to utilize X-ray CT in order to probe the pathways of oxygen as it exits the electrolyzer. Typically, titanium would be used as the anode-size porous transport layer, however x-rays attenuate too much due to titanium's high atomic weight of 47.867 amu. Carbon has an atomic weight of 12.0107 amu, which is approximately four times

less than that of titanium. Figure 6 shows an example of disassembled electrolyzer with sintered Ti as a PTL. Using the treated Freudenberg at the anode allowed us to gather both morphological and temporal information on oxygen's transport in these model electrolyzers. The cathode catalyst layer was untreated Freudenberg GDL. The anode and cathode bipolar plates were made of graphite, as operating time of electrolyzers was only several hours and therefore low corrosion currents were observed from using carbon PTL and carbon bipolar plates. Our earlier study proved that it is possible to operate with carbon PTLs for a short duration without significant carbon corrosion⁹.

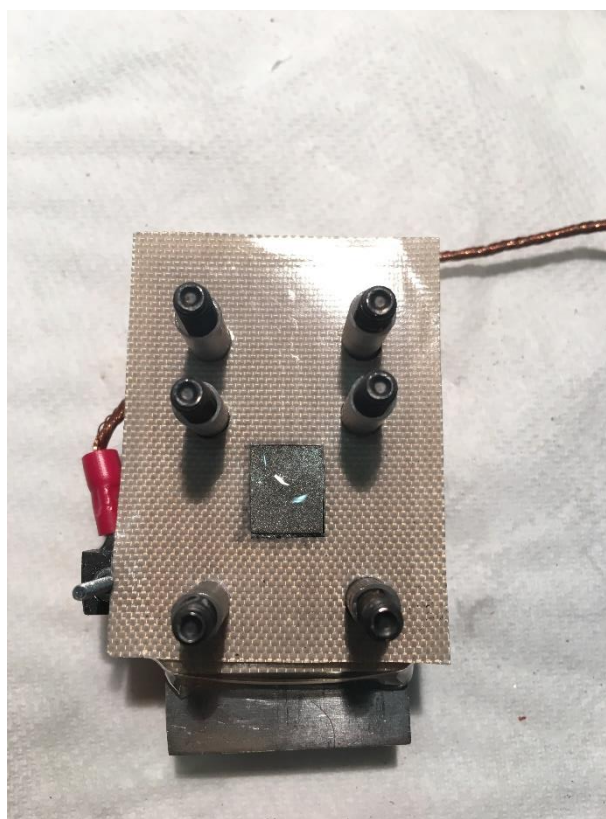


Figure 7. A disassembled electrolyzer cell, with titanium PTL (middle) wetted from testing, and Teflon gasket exposed.

2.3- Operando Cell Design

Due to the rotation needed during X-ray CT experiment at the beamline, it was necessary to design an operando cell with the limitations associated with the beamlines in mind. The *operando* cell²³, consists of four aluminum plates, two BPPs, two PTLs, a Teflon gasket, a CCM masked with Kapton tape, and compressed together with anodized aluminum bolts. The graphite BPPs (Fuel Cell Store, College Station, TX), were chosen as they do not attenuate significantly x-rays. Figure 8 shows an assembled and exploded view of the electrolyzer hardware used for X-ray CT imaging.

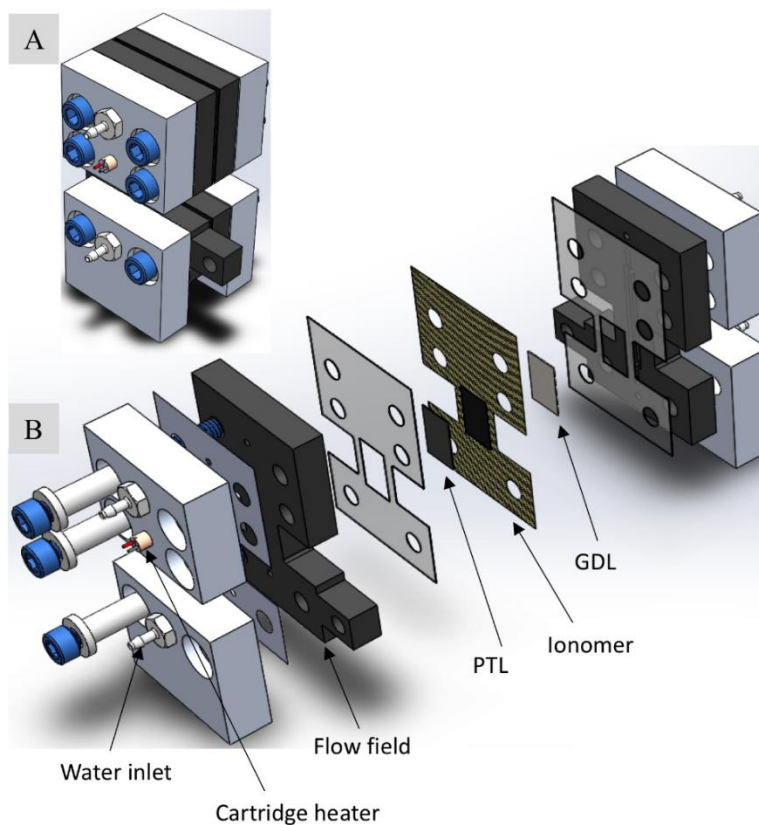


Figure 8. (A) the fully assembled PEM electrolyzer cell, and (B) the exploded view of the PEM electrolyzer cell, with the GDL, PTL and ionomer (PEM membrane) noted.

The aluminum plates and BPPs were machined to provide a 2 cm long vertical x-ray transparent window for imaging. The BPPs were machined with a micro-mill, and in addition to the x-ray transparent window have two parallel channels 1mm x 1mm in area as well as a 1mm land between the two channels. The cells are first assembled by cutting out a 2cm² piece of CCM and masking it to 1 cm² active area with 20 um Kapton film. Next, the PTLs were cut slightly larger than the active area of the CCM, in order to ensure that the active area would be covered completely during operation. The hard-stop PTFE-reinforced fiberglass gaskets were used on anode and cathode side of the electrolyzer to achieve 20 % compression on the cathode and 50 % compression on the anode. Finally, the entire cell is assembled, with special attention paid to ensuring that the CCM is evenly compressed to ensure as little ohmic resistance as possible. Six anodized aluminum bolts with extra peek washers were used to compress the cell. Multimeter was used to measure cell resistance after compression, if the resistance was several ohms, we know the cell was shorted and it had to be reassembled. The current collector leads were attached with bolts to the sides of the graphite plates that were machined to accommodate this addition. Then the set-up connected to tubing to a syringe pump and electrically to a potentiostat, as well, as cartridge heaters and thermocouples to provide heat flux.

2.4 – Electrochemical Characterization and Operation

The cell was connected to a Gamry 5000E potentiostat (Gamry Instruments, Warminster, PA) to apply current densities and measure potentials. Water was supplied on the anode side via a syringe pump (Harvard Apparatus, Holliston, MA). The syringe was filled with 40 mL of deionized water and connected to the cell via 1/8” tubing to the anode; another piece of tube would lead to a nearby container to collect unreacted water. The heat was applied with two cartridge

heaters, the K-type thermocouples measured temperature on the top of the aluminum plate. A PID controller was used to apply a set heat flux to the cell²³. After each cell assembly a resistance across the cell was measured to ensure that it was not shorted. Once we ensured that water was flowing through the cell and that the temperature was stable, we first took an OCV tomography scan in order to get a background scan for future reference. Next the potentiostat was set to the desired current density and the tomography or radiography scans were collected. The experiments varied from constant currents of 1 A to 4 A, and 1 mlpm to 3 mlpm in increments of 1 A and 1 mlpm for current and water, respectively. For each tomography or radiography run, a polarization curve and electrochemical impedance spectroscopy (EIS) experiments were performed; the latter was primarily to check that the ohmic resistance was still within an acceptable range.

2.5- Image Processing and Visualization

Due to the rotation necessary to gather the images, the radiography projection images acquired during scanning need to be reconstructed. The raw data for both tomography and radiography is collected as radiography. These data sets are then reconstructed into a 3D tomography data set by converting them into Fourier space with a Fast Fourier Transform (FFT), and the result is a sonogram. Next, the inverse of the FFT is taken to convert the sonogram back into real space. These tomographic reconstructions were made by utilizing Tomopy and the Grideric algorithm and were typically completed while at the beamline.²⁴ In order to reduce the image stack size, the stacks were converted from 32-bit to 8-bit utilizing a javascript in Fiji/ImageJ. It should be noted that for every image stack they had to be converted using the same grayscale range so that each stack could be comparable to one another during further data analysis.

After converting to 8-bit with the same grayscale values, cross-sections from different perspectives of the stacks were taken in order to both visually and computationally quantify the differences in oxygen content generated at varying current densities as well as with different flow rates, as well as whether or not oxygen takes preferential pathways through the electrolyzer's PTLs. Since the sample is rotating during data acquisition, there are minor differences between each stack; these differences, i.e. the slice that one prominent feature was on could vary by up to twenty five slices, were important to note so that all the same slices could be taken for further investigation, which is detailed in Chapter 3 and the results are discussed in Chapter 4.

2.6- Machine Learning with Weka Algorithm in ImageJ

As discussed in Section 1.6, machine learning was an integral part of this study. The specific machine learning software was an ImageJ package known as the Waikato Environment for Knowledge Analysis (Weka); it is an opensource plug-in specifically created for the classification of large sets of images²⁵. As it is a supervised machine learning algorithm, it requires the user to select and categorize the areas of interest on a given image. Essentially, the user is telling the algorithm which grayscale values belong to which category. In the case of this study, oxygen content versus non-oxygen areas was of the most importance. The area of interest was selected from the stacks- i.e. the set of slices containing images of the porous transport layer- and were adjusted so that the brightness and contrast were the same for every new stack.

After adjusting the brightness and contrast, a single stack was opened in the Weka interface. From there, selections from slices from the beginning, middle and end of the stack were classified by hand. After classifying the slices of interest, the algorithm was used and a classified stack was produced. The accuracy of the first run was lacking, and therefore multiple runs are

needed before the accuracy of the algorithm is sufficient; the accuracy is easily determined by comparing the classified slices with the original slices by eye. In Figure 10, examples of slices pre and post segmentation training in Weka are shown, where the red areas are classified as oxygen and the green areas are either fiber or water. In order to achieve the level of accuracy required, the classifier was trained four times, with more slices classified by hand in order to further increase the accuracy. This iterative process was necessary, as the grayscale values between oxygen and non-oxygen areas in the porous transport layers were relatively close, thus making it difficult for the algorithm to differentiate between the two categories in the first two runs.

Once the algorithms were trained, the next step was to apply the final algorithm to the entire stack. This was done by splitting the original stack containing the PTL into two and analyzing them with the same algorithm in parallel. This was done on 64 Gb RAM computer stations and splitting stack in two of 2000 images ensured higher computational efficiency. This process was repeated for every test, resulting in a red and green image stack that was then converted into binary for processing via the z-project function in ImageJ. An additional step taken prior to utilizing the z-project function was to collapse the pixel values to be between 0 and 1- this served two purposes: the first was to simplify the z-project calculations and the second is to make later interpretation in Matlab easier. After processing, the resulting z-projects for the different tests were made into 3D meshes for both qualitative and quantitative analysis, the results of which can be seen in Chapter 3.

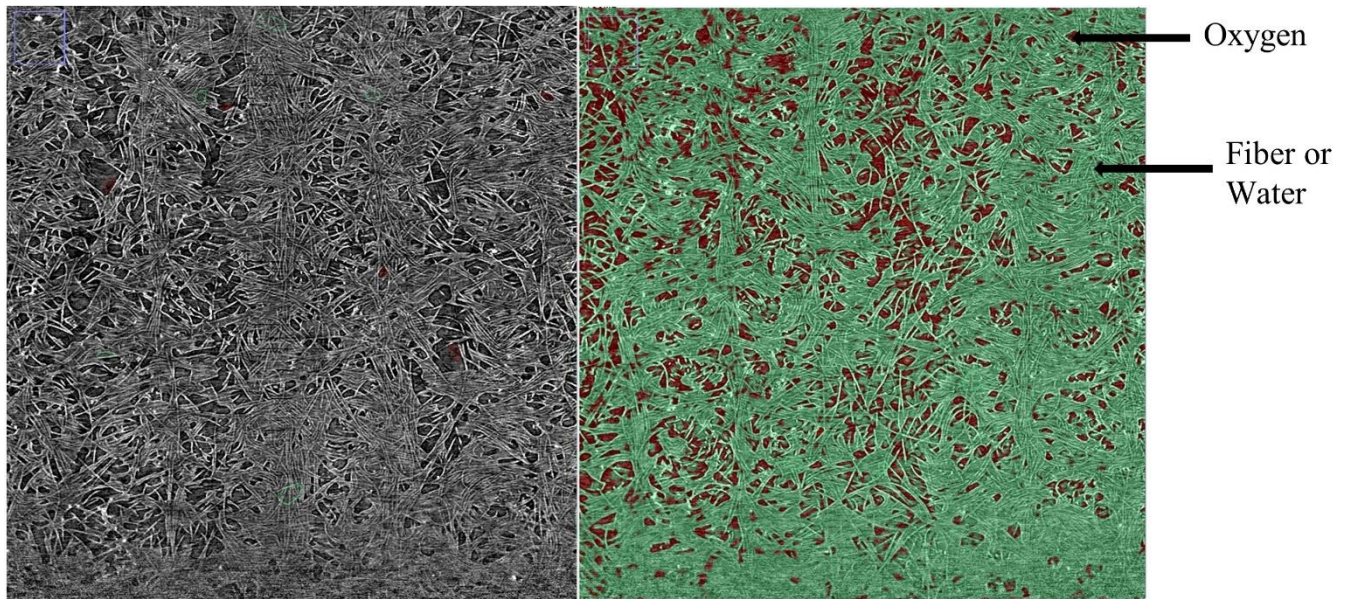


Figure 9. Examples of images pre(left) and post(right) processing with Weka. Post processing, the image is segmented into areas of oxygen, in red, and areas or either water or fiber which is displayed as green.

Chapter 3. Data Interpretation and Additional Details

3.1-Chapter Introduction

In this chapter we focus on explaining how to interpret X-ray CT data and provide additional information on data quantification. We start by showing a 3D view of electrolyzer and examples of grey-scale cross-sections that show both oxygen and water within the PTL. Then we provide additional detail on computations of oxygen content within the PTLs that required knowledge of along which direction the data was quantified.

3.2- A Guide to Interpreting Tomography Data

Since tomography data is in 3D, it can be difficult to interpret to someone who is not accustomed to X-ray CT. As such, throughout the remainder of this thesis, please reference the

visual guides in this section to better understand and interpret tomographic data.²⁶ First and foremost, it is important to note the labels used to reference the types of views used to analyze this 3D data. Figure 8 shows representative 3D volume rendering of an electrolyzer. It also shows three cross-section planes that will be used to represent data with grey-scale images. The x-y plane is through-plane view where one can see both channels, the cathode GDL, the PEM membrane, and the anode PTL in the same slice. A ‘slice’ is essentially a single image that is used to build up the 3D data. This front-facing slice was used to determine the oxygen content along the length of the anode-side PTL. The next most used view is the x-z plane, which is the in-plane view; this perspective can be thought of as a top-down view through the 3D data. The x-z plane was used to develop the Weka learning algorithm in order to interpret the oxygen content throughout the PTL and is therefore one of the most important views for this project. In addition to using the x-z plane for interpreting the oxygen content in the PTL, it was also used with the z-project function in ImageJ to build an average of the amount of oxygen vs the catalyst distribution. Finally, the y-z plane, while not used as much as either the x-y or x-z plane views, was used to understand how the oxygen content changed within the length of the PTL. By area-averaging information in y-z plane we found oxygen content under land vs that under channel. It is used mostly to quantify land-channel effects on oxygen distribution.

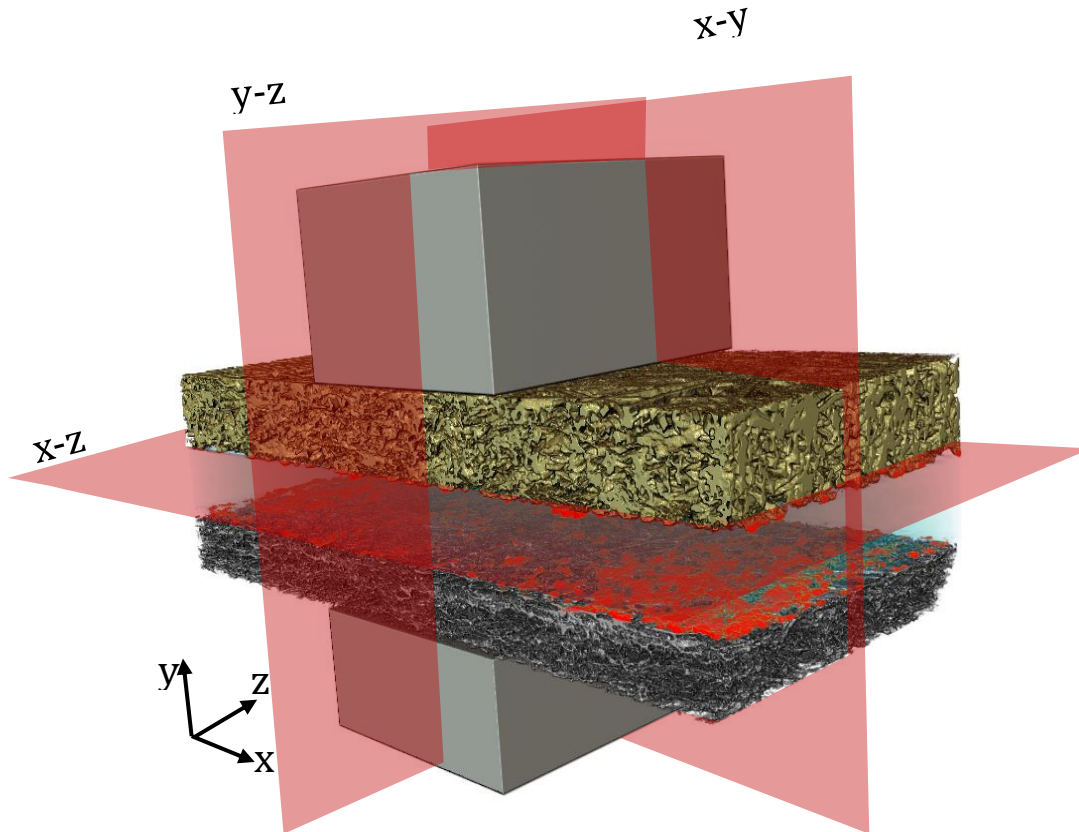


Figure 10. A 3D representation of a traditional PEM electrolyzer, where the relevant views examined in this study are noted in red. The Ti PTL is in yellow, and the carbon paper GDL is in gray.

Figure 10 shows representative grey-scale cross-sections for each of the planes: x-y, y-z and x-z. In this study mostly x-y and x-z planes are used for oxygen visualization, whereas y-z is used mostly for oxygen quantification. The bright locations on the image are catalyst layers, as these consist of the most X-ray attenuating materials (Ir and Pt). Oxygen appears as dark, as it is the lightest element in the electrolyzer. Water and carbon have very similar X-ray attenuation and therefore it is difficult to separate them. In this study a single phase will be used to identify both.

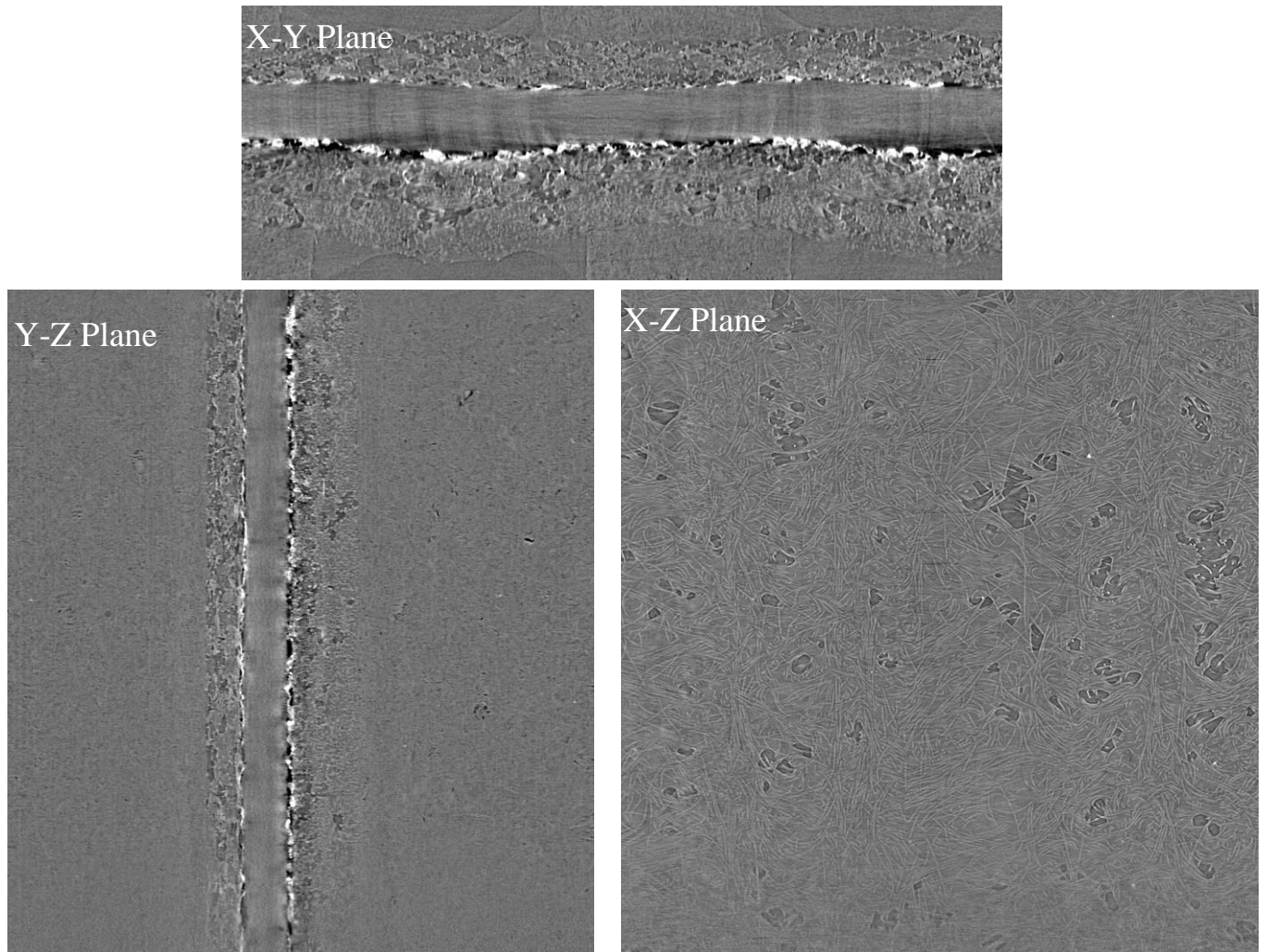


Figure 11. Labeled cross-sections detailing how to interpret the tomography cross-sections in different points of view. All z-projects, and Weka training were done with x-z plane slices.

3.3- Oxygen Content Measurements and Visualization

As discussed in Section 2.5 the oxygen content measurements come from the top reslice view, as this was the best way to capture oxygen content in the anode-side model PTL. This process selecting each section of slices for Weka to segment went as follows: First, the whole stack-i.e. all slices for that test- was put into the top reslice perspective. Next, the section where the anode-side model PTL was present were cut from the whole original stack; this was to reduce the amount of

time it would take Weka to segment the individual stacks, as it is a computationally demanding process and any unnecessary slices present could cause the program to crash. From there, the stacks containing the anode side model PTL slices were split in two, in order to reduce the computational burden on the program. These split stacks were processed in parallel, on separate machines in order to maximize the number of stacks that could be processed at the same time. This process was repeated until every test of a different flowrate and current density were segmented. One stack of approximately 100 slices could take up to 7 hours to complete, due in part to the complexity as well as the size of the stack.

After segmenting the stacks, the originally split stacks of the same test were recombined in ImageJ for interpretation. For each test, the following measurements were taken through-thickness oxygen content, length oxygen content, and Z-projects of the top reslice view to visualize the oxygen content distribution. For the z-projects, it is important to note that the pixel values have to be between 0 to 1, and to do this it was necessary to use the divide function in ImageJ; in all tests, the pixel values were divided by 255, as that was the highest value of the pixels from the Weka results. From there, the contrast of the image was adjusted such that the pixel values were still from 0 to 1. Once this was complete, the z-project function was used. The z-project function essentially sums up the pixel values in each direction, and in our case, it was from the z-direction from the top reslices. The results z-project images- as well as the oxygen content results- were made into 3D meshes in Matlab. It should be noted that because the meshes are 3D, we had to choose a 2D perspective in order to better understand the oxygen distribution; in our case, we used the x-y axis view of the 3D mesh. A similar process was used to visualize the anode-side catalyst distribution, to compare the catalyst distribution to the oxygen content distribution.

In addition to the z-project and length and through-thickness oxygen content measurements, a correlation coefficient calculation was done. In Matlab, the function $R = \text{corr}(A, B)$ was utilized to determine if there was any correlation between the catalyst distribution and the oxygen content of different tests. This was repeated between different oxygen content tests from 1 A to 4 A, in order to verify that there was a statistically significant correlation between the catalyst and the oxygen content.

Chapter 4- Results

4.1- Chapter Introduction

In this study we focus on the influence that flowrate and current density have on the oxygen content of the PTL. X-ray tomography provided the raw data necessary to qualitatively and quantitatively study oxygen content in the PTL. Image processing in ImageJ and machine learning with Weka provide quantitative analysis of the oxygen content in the PTL, whereas the polarization and EIS curves provide electrochemical data on the performance of the cells while in operation. We quantify the oxygen content in the PTLs at different flowrates and current densities. Lastly, we build correlation between oxygen content in the PTLs and catalyst layer.

4.2- Electrochemical Polarization and Characterization

Figure 12a shows polarization curves, which are potential as a function of the applied current density. The polarization curves were recorded between 0 and 6 A and three water flowrates 1, 2 and 3 mlpm. We observe similar polarization behavior between the three conditions, indicating that the water flowrate did not have significant effect on electrolyzer performance. We also observe relatively high voltages (5 V at 5 A). To explain this high potential we study the Nyquist plot,

shown by Figure 12b. From Figure 12b the real-axis intercept that corresponds to high-frequency resistance (HFR) of electrolyzer can be extrapolated to be 0.6 to 0.8 Ohms. At 5 A, which is a high current, the voltage drop due to Ohmic loss for a cell with 0.6 Ohm will be 3 V. Thus, a large contribution to the cell potential is Ohmic loss. Part of it is the thick membrane, which is Nafion 117 or 180 μm thick and another part of it is higher contact resistance at interfaces due to in idealities of the cell design. 2 mlpm flowrate showed higher HFR and also bit worse polarization behavior.

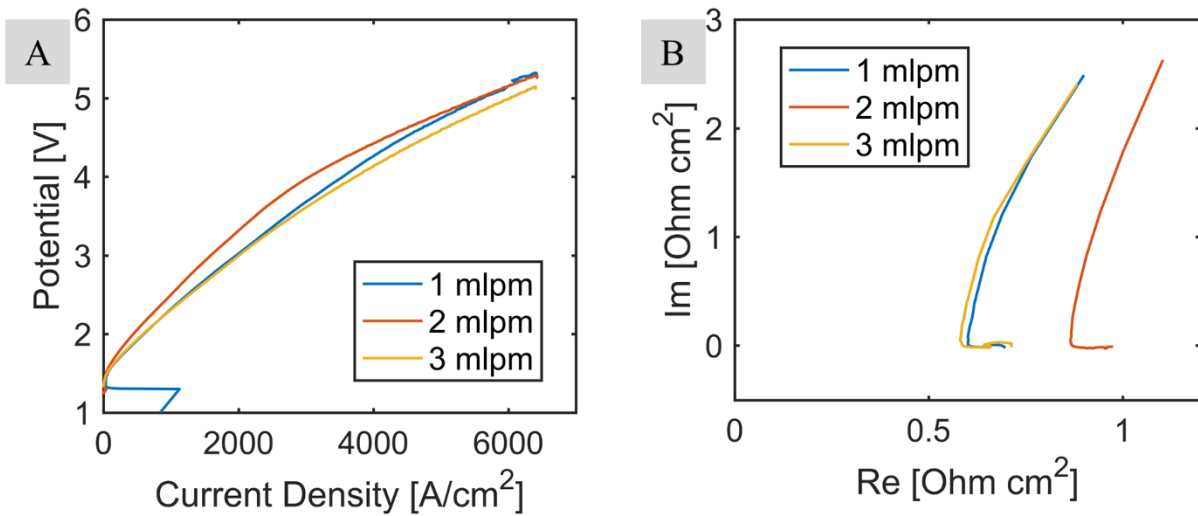


Figure 12. Polarization(A) and EIS (B) of the cells prior to in-situ x-ray computed tomography.

Figures 13 and 14 shows the potential as a function of time across the applied current densities and water flowrates. The maximum current density used in this study was 4 A. We varied the applied current density from 1 A to 4 A. For each applied current density, the flowrate was varied from 1mlpm up to 3mlpm. Prior to imaging, the cells are conditioned and checked for performance. Figure 13a shows that for three flowrates the potential was around 2.5 V for the measuring time between 10- and 20-min. Figure 11b shows potential of the cell being around 3 A for the three water flowrates. For 3 and 4 A, as shown by Figure 12 a and b, respectively, we see

an initial increase in potential for water flowrates of 0.5 and 1 mlpm but eventual decay in potential with time for this water flowrate. This is indicative that there is relaxation in the electrolyzer, and better performance is achieved at lower water flowrate with time. Overall, the polarization curves and constant current holds suggest that electrolyzer performance is not significantly affected by water flowrate.

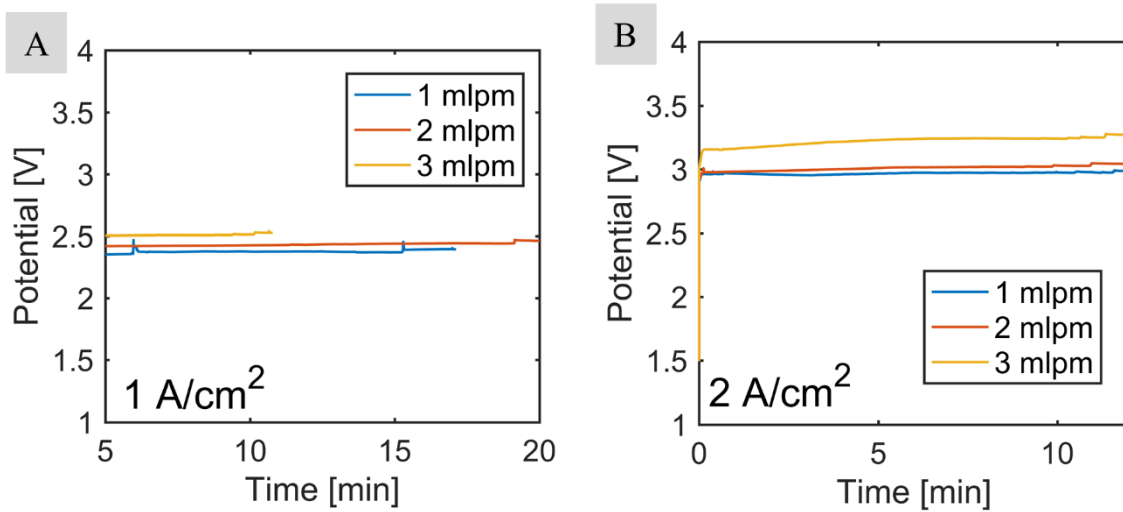


Figure 13. Potential holds during testing, ranging from 1A(a) through 2A(b), for each flow rate.

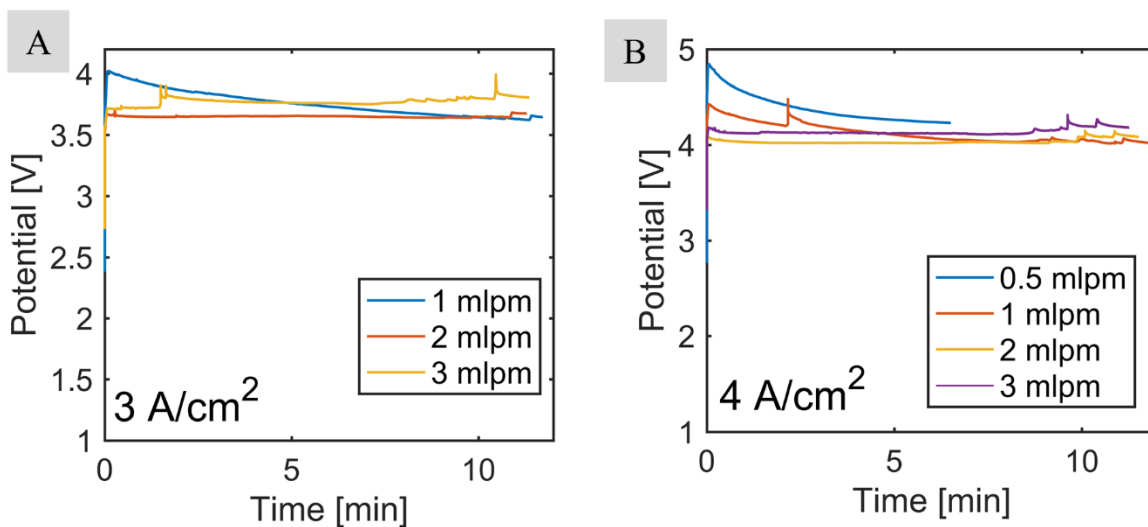


Figure 14. Potential holds during testing, ranging from(A)3A to 4A for each flowrate.

4.3- Cross-Sections of Grey-Scale Images of Electrolyzer Under Varied Current Densities and Water Flowrates

First, we image electrolyzer under open circuit voltage (OCV) condition to observe whether there any residual oxygen trapped within the electrolyzer. Figure 13 shows a cross-section image of electrolyzer at the OCV. Most of the PTL is filled with water and only in few locations we observe oxygen or air. This image proves that piranha solution treatment of PTLs was successful and the PTL turned out to be mostly hydrophilic. From this figure we can also observe that the PTL under the land is more compressed than under the channel. This is to be expected, as we compressed the PTL by 50 % to achieve pore sizes comparable to those of Ti PTLs. The cathode PTL showed lower degree of compression than cathode, as expected, as we targeted 20 % compression on the cathode.

In Figures 15, 16 and 17, x-y plane views can be seen for tests run at OCV, 1A and 4 A; these cross-sections were selected as they demonstrate visually that the oxygen content- seen as ‘voids’ present within the PTL. Both figures show cross-sections for three water flowrates. Figure 12 shows that oxygen content in the PTL did not change as water flowrate increased from 1 to 3 mlpm. We observe several locations where oxygen goes through from catalyst layer to the channel or land. Furthermore, we do not observe any trend in oxygen concentration in PTL under land vs. under channel. There seem to be very little correlation between oxygen concentration and land channel location or any other geometrical feature. Comparing Figure 14 at 1 A to Figure 13 at OCV, we observe significant amount of oxygen present in the PTL when current density is applied compared to that under OCV.

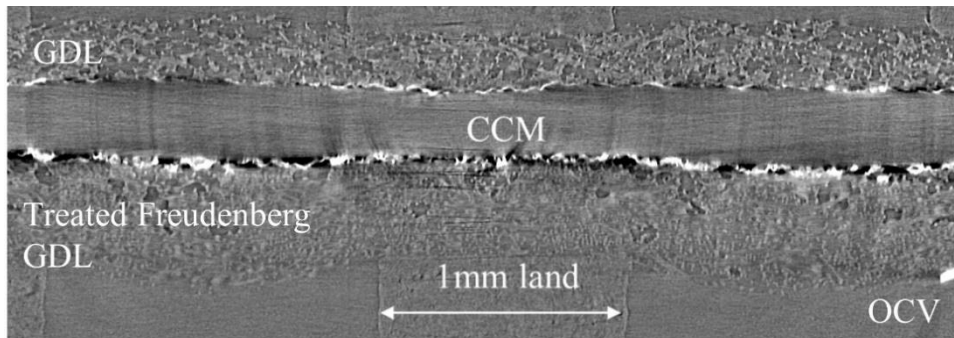


Figure 15. X-Y plane view of an electrolyzer at OCV. It is important to note that the PTL, which is a treated Freudenberg GDL, is saturated with water.

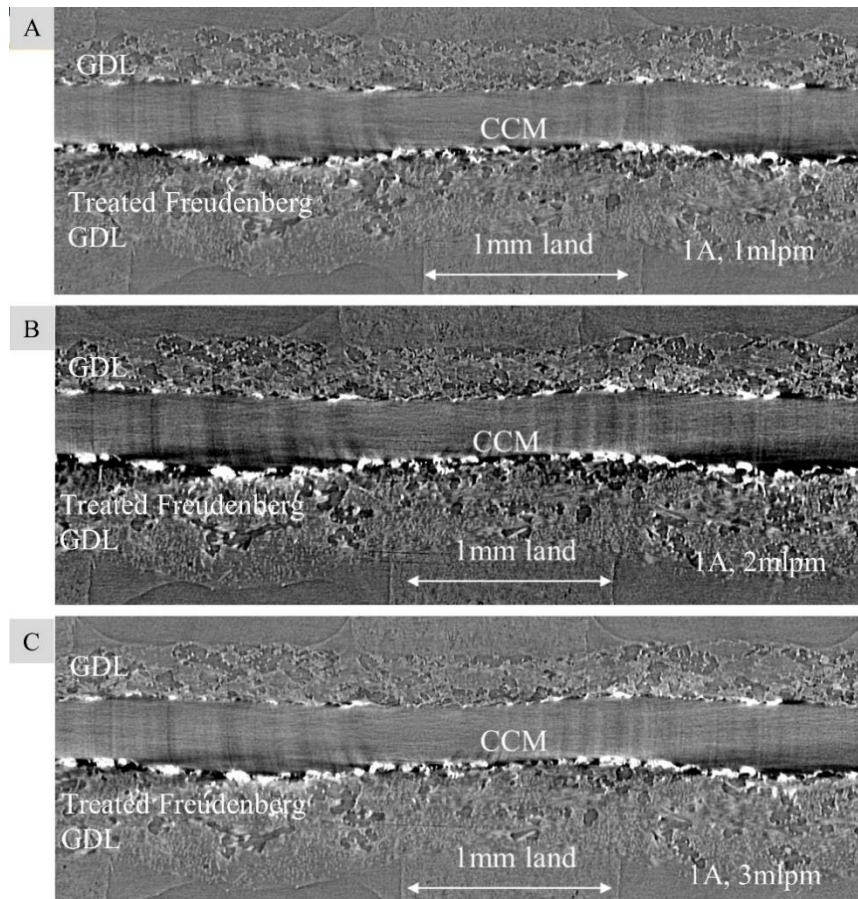


Figure 16. X-Y plane view of the PEM electrolyzer during operation, where (A) is 1A 1mlpm, increasing up to (C) of 1A and 3mlpm.

Figure 14 and Figure 15 appear virtually identical, although current densities are significantly different between the two figures. Oxygen seems to follow the same pathways at 4 A as at 1 A. No new pathways emerged for oxygen removal. Although these images are only 2D we can already observe that oxygen seem to follow the same pathways through the PTL, regardless of current density or water flowrate.

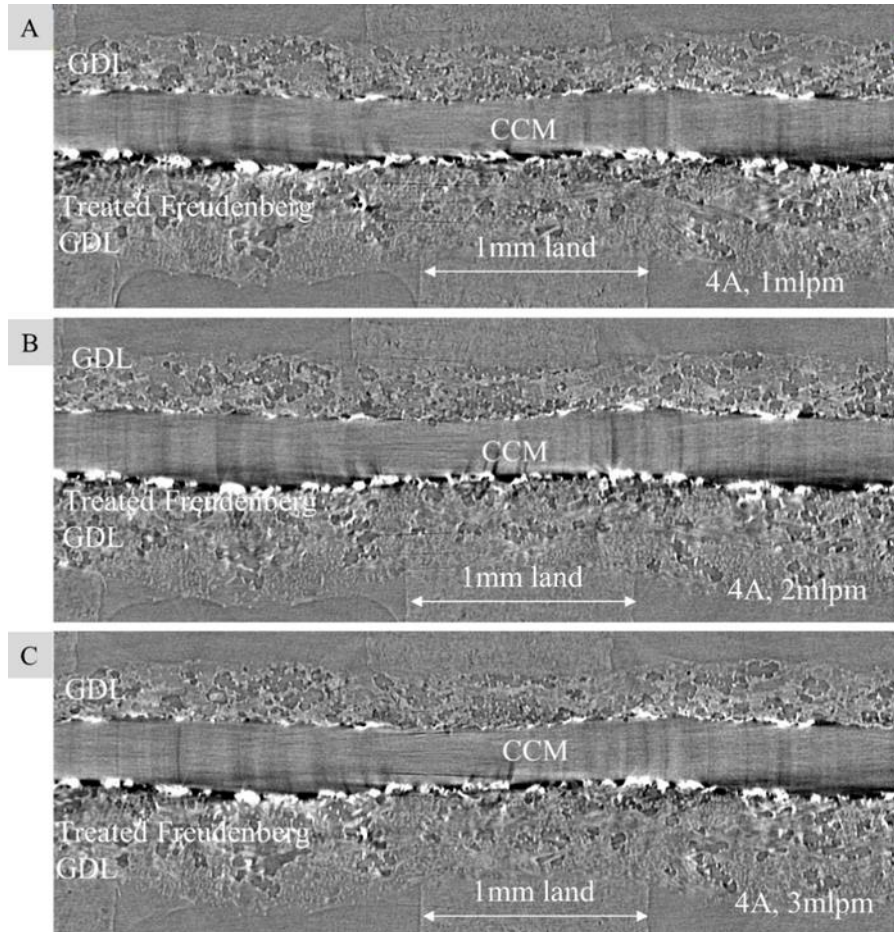


Figure 17. X-Y plane view of the PEM electrolyzer in operation, where (A) is 4A 1mlpm, (B) 4A 2mlpm, and (C) 4A 3mlpm.

In Figures 18 and 19, x-z plane views of the PTL at 1A and 1mlpm, and 4A and 3mlpm respectively, were taken. The sections labeled as channel and land correspond to the channel and land areas labeled in Figures 11-15 and are demarcated with red dashed lines. Figures 18a and

19a both show the PTL close to the land and channel (further away from the PEM), and Figures 18b and 19b show the PTL close to the catalyst layer. Visually, there is more oxygen present in the PTL when closer to the catalyst layer than in the PTL closer to the land-channel area. This follows our expectation that oxygen is more concentrated closer to the catalyst layer, as this is where it is evolved. However, we do not see significant oxygen content differences for 1 A vs 4 A near the catalyst layer. The bright areas on the edges of the fiber in Figures 18b and 19b is catalyst, and this is expected as closer to the catalyst layer the catalyst would be present. In addition, it should be noted that even at the extreme ends of our experiment- i.e. 1A and 1mlpm vs. 4 A and 3 mlpm- there is a general trend towards oxygen becoming trapped beneath the land. We observe more oxygen trapped under the land at 4 A and 3 mlpm compared to 1 A and 1 mlpm. It is trapped in the same land location but fills more PTL pores. At higher flowrates, we would expect that the oxygen would still be removed by water, but even at 3 mlpm there is still a considerable amount of oxygen trapped beneath the land. This is consistent with findings from a recent publication by Maier et al, where they combined x-ray computed tomography and neutron radiography to analyze mass transport in PEM electrolyzer liquid-gas distribution layers. During their study, Maier et al noted that there was more oxygen trapped in the land- referred to them as ribs- rather than being present in the channel.²⁷

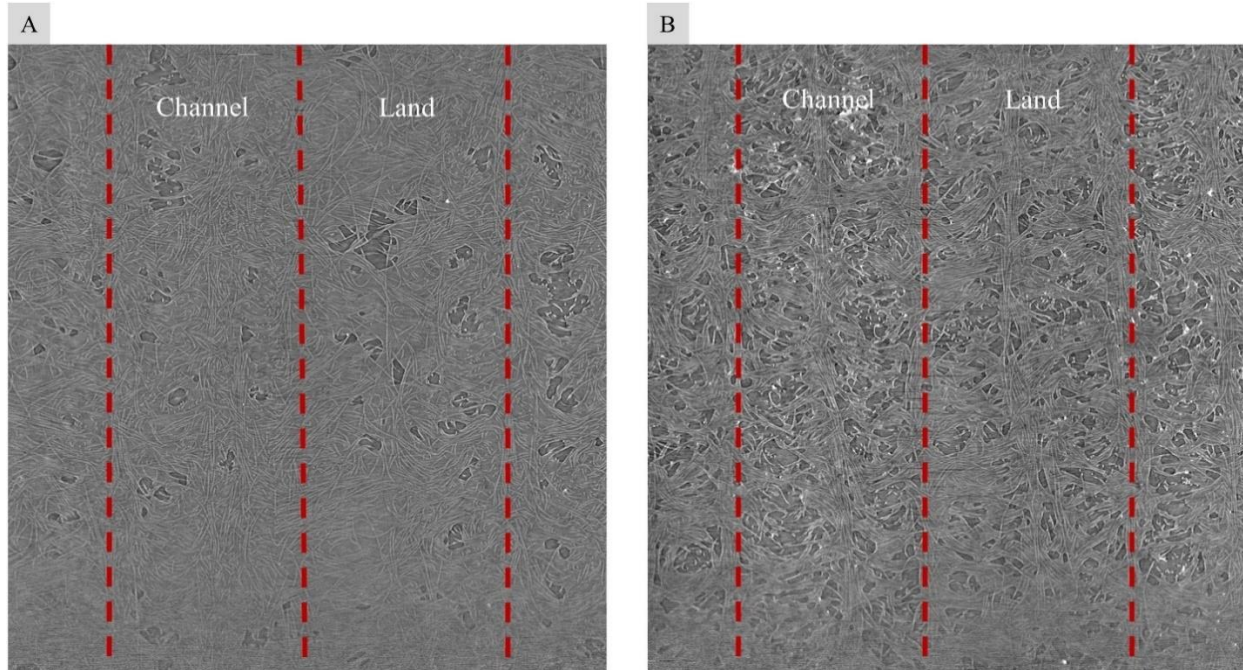


Figure 18. X-Z plane view of the PTL during operation at 4A and 3mlpm, where (a) is a cross-section taken near the land and channel, and (b) is a cross-section taken near the catalyst layer.

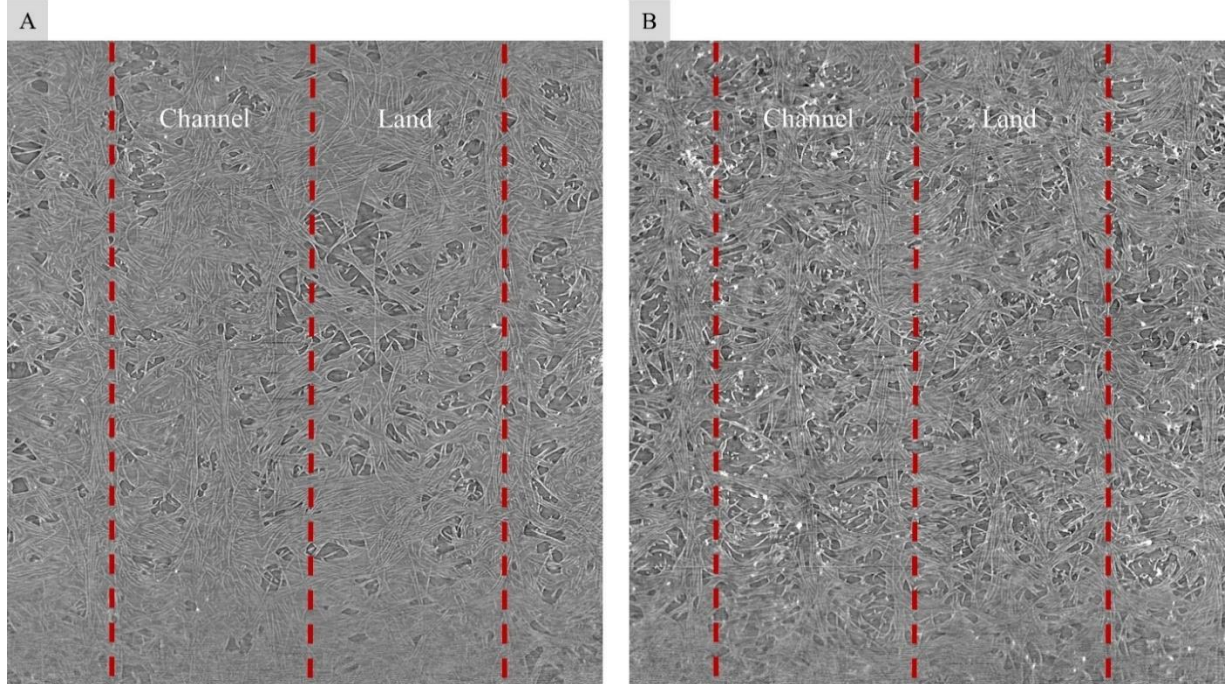


Figure 19. X-Z plane view of the PTL during operation at 1A and 1mlpm, where (A) is a cross-section taken near the land and channel, and (B) is a cross-section taken near the catalyst layer.

Although Figures 18 and 19 demonstrate a general trend towards oxygen becoming trapped beneath the land even at higher flowrates, with visual inspection it is difficult to quantify. Oxygen fraction within the PTL as a function of PTL position is quantified and shown as Figure 20, where four current densities are shown at different flow rates $x = 0$ location indicates the PTL contacting catalyst layer, whereas $x = 320$ μm shows the location where PTL is near land and channel. The shaded area beyond the 320 μm shows the uncertainty in the algorithm due to difficulty to quantify oxygen content within the channel. For 1 A we observe oxygen content near catalyst layer to be between 30 and 40 % within the PTL. Then in the middle of PTL it decreases to about 15 % and near the channel it varies from flowrate to flowrate. For the cell measurements at 1 A the cell was not fully conditioned, hence we observed more oxygen near the catalyst layer, compared to operation at higher currents. At 2 – 4 A oxygen content near the catalyst layer was 20 – 30 % and it decreased to 5 % near land- channel location, after which it increased again when entering the channel. Again, we do not see significant variation in oxygen content within these cells with water flowrates.

Figure 21 shows the same data as in Figure 20 but with constant flowrates and varied currents. Again, there appears to be no correlation between current density and oxygen content within the PTL. Zlobinski et al. built upon the earlier Seweryn et al. study and did a more thorough quantification of water saturation in the PTL with neutron radiography. First, they confirmed the earlier Seweryn et al. study that oxygen content in PTLs did not change with current density from 0.1 to 2 A/cm². Then, they showed that near the catalyst layer water saturation is 0.5, therefore oxygen content is 0.5 too. In this study oxygen content is slightly lower of 0.2 to 0.4 compared to their study. It should be noted, that their PTL is 1 mm, and therefore oxygen diffusion length is longer which results in a larger accumulation of oxygen near the catalyst layer. In addition,

Zlobinski et al. also observe oxygen content dropping to 0 near the land-channel location, this is in a good agreement with our findings.

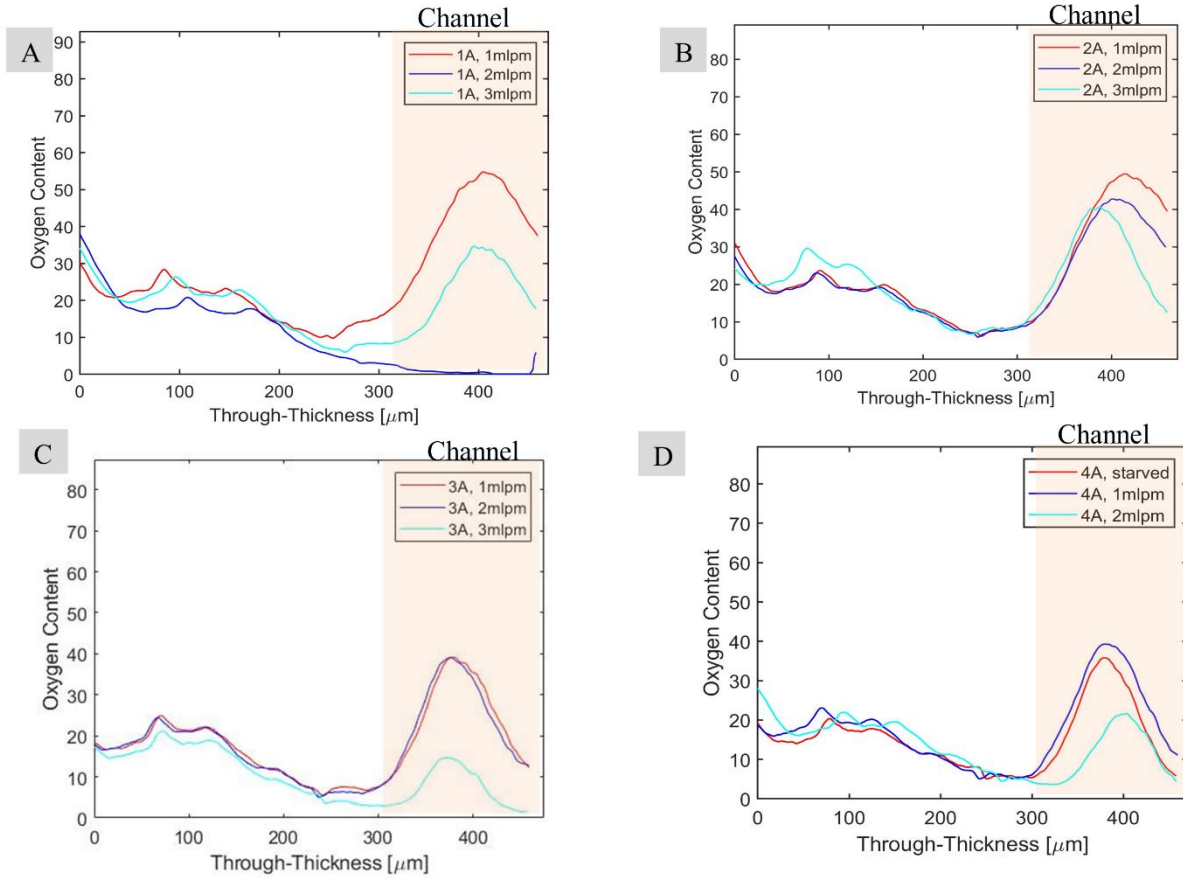


Figure 18. Oxygen content as a function of through-thickness PTL location for constant current densities and varied flowrates. The location of the channel is noted with the orange box and label.

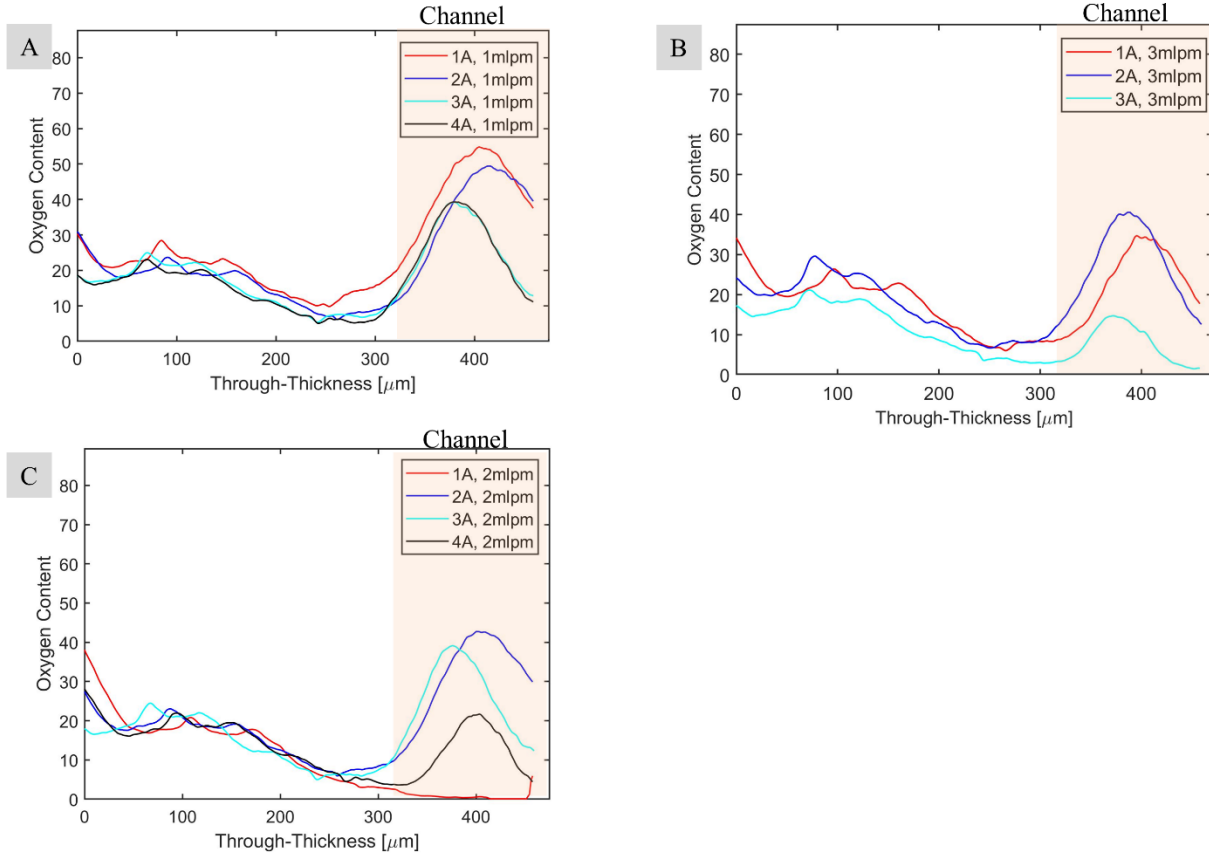


Figure 19. Oxygen content figures comparing the through-thickness for varied current and constant flowrates. The location of the channel is noted with the orange box and label.

Figure 22a shows oxygen in-plane concentration for 3 A and three flowrates, whereas Figure 22b shows oxygen content in the PTL where the current densities varied but the water flowrate of 1 mlpm was constant. This data represents oxygen content in PTL near the land and channel locations (as shown by the orange area in Figure 21), only 1/3 of PTL thickness was used to generate this data. The red dashed lines connect to the bright areas of the x-y plane cross-section below, where the bright areas correspond to the catalyst. Peaks in the oxygen content across the length of the PTL are observed periodically, regardless of the flowrate. The oxygen peaks appear every 400 ums. The peaks oxygen fractions varied from 12 to 25 %, whereas the oxygen fraction valleys varied from 2.5 to 7 %. Interestingly for 1 A and 1 mlpm the peaks in

oxygen concentration are not pronounced and oxygen content varies between 15 and 20 %. As mentioned before, at 1 A the cell was not fully conditioned and hence the results are different from the other results from subsequent testing. The oxygen distribution at 3 and 4 A shows virtually similar trend. What we can conclude that when exiting the PTL oxygen arranges into the channels that are 400 μm apart and then either is trapped under the land or leaves through the channel.

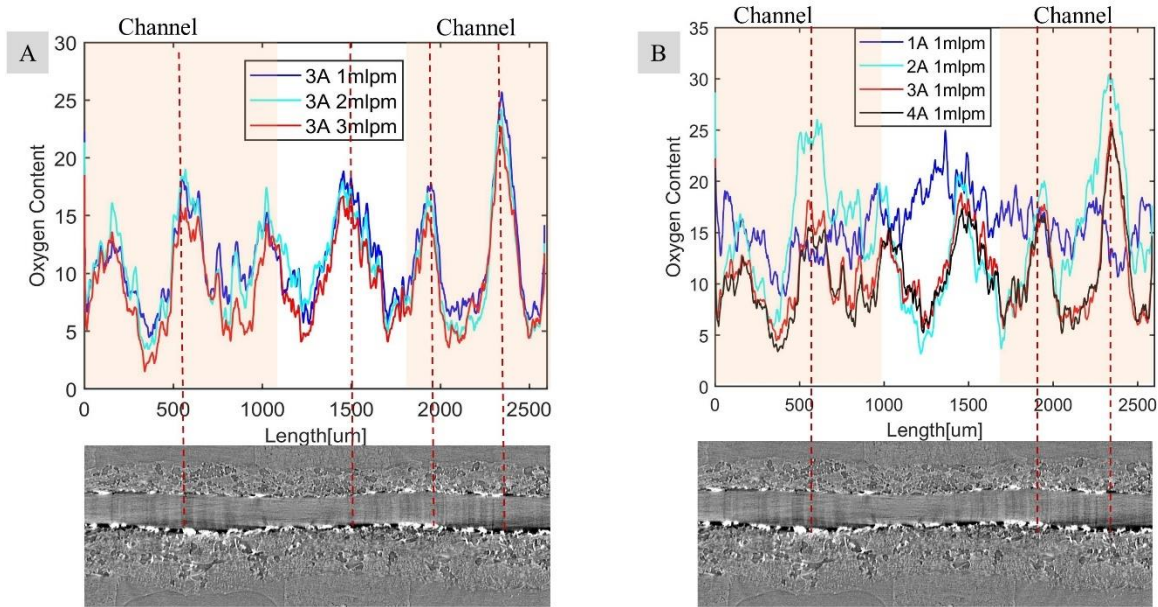


Figure 20. Oxygen content measurements along the length of the PEM electrolyzer, where (A) compared the same current density at different flowrates and (B) compared different current densities at the same flowrate.

Figure 23a-c shows the same data as that in Figure 19 but represented in 2D by using the z-project method described in section. The data from the last 1/3 portion of the PTL near land and channel was collapsed into one slice. Figure 23d-f shows z-projects of the catalyst layer, where the catalyst layer was adjusted, and the information was combined into a single image. Z-projects are produced in ImageJ by adding the pixel values in a chosen direction- in this case, these z-

projects were produced from x-z plane views, for both the oxygen content and the catalyst distribution. Figure 23 shows the x-z plane of the collapsed data and it compares the oxygen content and the catalyst distribution. Areas that are red indicate a higher oxygen content, and in the bottom row of figures the red indicates a higher density of catalyst present. As shown in Figure 22, there appears to be a periodicity in the oxygen content in the PTL near land-channel location, and this is shown in 2D in Figure 23. Figure 23a-c shows that local oxygen content can be as high as 70 %, in certain locations mainly under the land (for 2 and 3 A). The periodicity is less defined for 1 A as we hypothesized that this periodicity is associated with the catalyst distribution, and this is roughly true when only considering the visual distribution of both oxygen and catalyst. We observe that the catalyst distribution in the catalyst layer is non-uniform with longer stripes of catalyst that by eye can be correlated to preferential oxygen pathways formation.

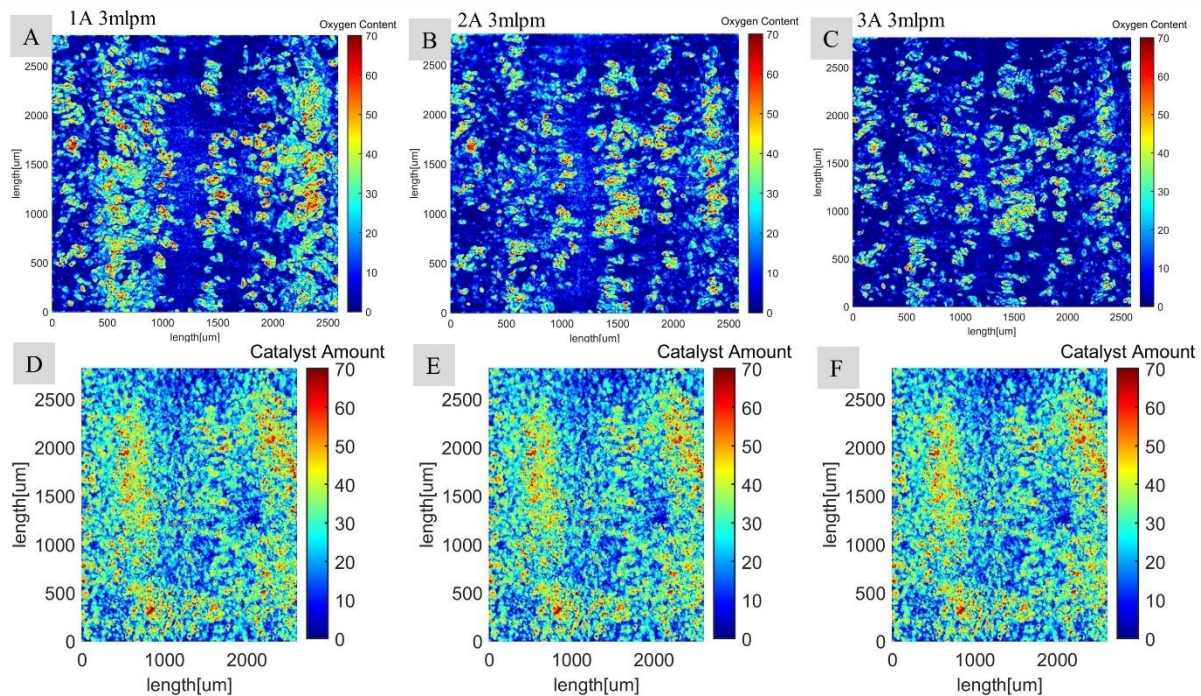


Figure 21. (A) through (C) are Z-projects of the x-z plane of the PTL at different current densities and the same flowrate, in the top row. (D) through (F) are z-projects of the catalyst layer.

Table 1 shows correlation coefficients between the data of different current densities and between oxygen content and catalyst distribution in the catalyst layer. A correlation coefficient of 1 and -1 indicates that the two images match, whereas correlation of 0 indicates that there is no overlap between the two data points. As shown in Table 1, there was little to no correlation found between the catalyst distribution and the oxygen content, as correlation coefficients are below 0.1. Therefore, there is likely another explanation for the periodicity of the oxygen content at the bottom of the PTL. This periodicity is perhaps due to oxygen taking preferential pathways as it exits the PTL, which would account for the apparent periodicity. Zlobinski et al suggests that the pore network inherent to a porous media- in their case it was sintered Ti- could account for the gas traps.²⁸ Gas traps, as defined by Zlobinski et al, are areas of either high hydrophobicity or hydrophilicity inherent to a porous media. These gas traps would explain the periodicity of oxygen content in the treated Freudenberg PTLs used in this study. However, it should be noted that there are differences in the materials used in the Zlobinski study from the ones used in our study; they used neutron radiography, and traditional sintered Ti PTLs, as well as thicker PTLs. Although Zlobinski and co-authors indirectly implied that oxygen takes preferential pathways, the current study has shown this phenomena directly with x-ray CT. Comparing the correlation coefficients for oxygen content between various current densities we observe strong correlation between 2 A and 3 A, and 3A and 4 A but weak correlation between 1 A and 2 A. This is, as we already mentioned, because the electrolyzer was not yet conditioned well.

A

Current Density and Flow Rate	Correlation Coefficient(R)
1A, 1 mlpm	-0.0207
2A, 1mlpm	0.0280
3A, 1mlpm	0.0390
4A, 1mlpm	0.0234

B

Current Density and Flow Rate 1	Current Density and Flow Rate 2	Correlation Coefficient (R)
1A, 1mlpm	2A, 1mlpm	0.0853
2A, 1mlpm	3A, 1mlpm	0.4633
3A, 1mlpm	4A, 1mlpm	0.6064

Table 1. (A) Details the correlation coefficients between the catalyst distribution and the different current densities, and (B) is comparing the current densities for the same flowrate for comparison to the correlation coefficients found for the catalyst vs current density.

Figure 24 is a schematic of our understanding of oxygen distribution within the PTL. Near the catalyst layer we observe higher oxygen content. As it transports through the PTL it forms preferential pathways that become more narrow as we approach land and channel, and then they become bit wider as oxygen either is stopped by the land or it is removed into the channel.

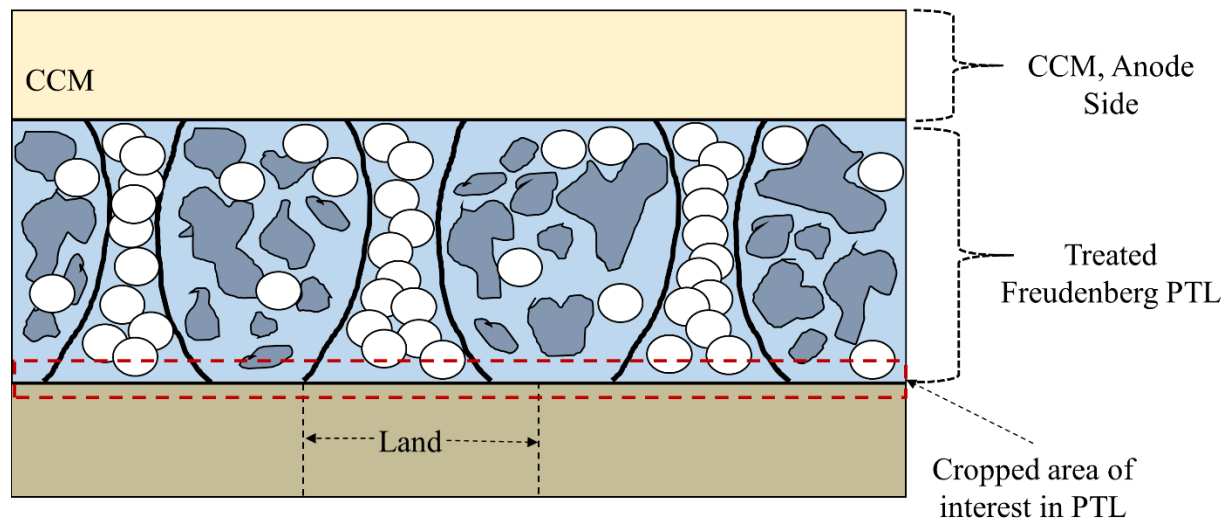


Figure 22. A schematic representation of possible preferential pathways represented by the funnel through the PTL. The area that was used to generate the oxygen content figures is highlighted by the dashed red box.

Chapter 5- Conclusions

In this study, we use x-ray computed tomography and machine learning to investigate the transport of oxygen in PTLs of PEM electrolyzers. We aimed to answer the question of whether oxygen transports through PTL and into the water channel via preferential pathway. In addition, we use electrochemical polarization and electrochemical impedance spectroscopy to quantify the performance of the PEM electrolyzer. We performed x-ray computed tomography on an MEA having $3\text{mg}/\text{cm}^2$ IrOx loading on the anode and Nafion 117 membrane, at different water flowrates and current densities. In this study, we used model PTLs that are Freudenberg carbon fiber layer treated with acid solution to become hydrophilic. The current densities varied from $1\text{A}/\text{cm}^2$ to $4\text{A}/\text{cm}^2$, and the flowrates increased from 1mlpm to 3mlpm. The first experiment was comparing the same slices of the highest current density (4 A) and lowest current density (1 A) to visually observe the distribution of oxygen. From the in-plane tomographs we observed that more oxygen was present near the catalyst layer compared to near land-channel location. Furthermore, we observed that at higher current densities more oxygen is trapped under the land location, compared to lower currents. Oxygen content varied very little with either flowrate or current density, however from a qualitative observation the oxygen appeared to take a preferential path as it exited the PTL. This trend became clear in the oxygen content measurements in the through-thickness direction and the along the x-y plane. In addition, there was a periodicity present to the oxygen content, with peaks appears at approximately every $400\ \mu\text{m}$. This trend was compared at varied current density

and constant flowrate, and constant current density and varied flowrate. These peaks range from 12 % oxygen content to a height of 25 % oxygen content.

Initially, these peaks were connected to areas where IrO_x electrocatalyst was densest. In order to make this comparison, z-projects were taken at 1A, 2A and 3A each at 3mlpm, and compared to the catalyst distribution. This comparison was both visual and quantitative, with the r-values calculated using the correlation function in Matlab. An unexpected result was that there was little to no correlation between the oxygen content and catalyst thickness, ranging from -0.0207 to 0.0234. To ensure that these correlation values were valid, correlation values were taken between 1 A at 1 mlpm and 4 A at 1 mlpm; except for 1 A 1 mlpm and 2 A 1 mlpm, there was an increase in the correlation coefficient to indicate a higher correlation. This difference we attribute to the fact that at 1 A the cell was not yet well conditioned.

Due to the lack of correlation between IrO_x electrocatalyst distribution and the periodicity observed in oxygen content, an alternative explanation is needed. A recent study by Seweryn et al observed a similar phenomenon when utilizing neutron imaging to visualize and quantify oxygen content in Ti PTLs at different flowrates and current densities, and proposed that oxygen takes preferential pathways as it exits the PTL, and this distribution is present regardless of the current density or flowrates used.²⁹ In addition, a follow-up study by Zlobinski et al. utilizing neutron radiography to visualize water content and transport in the PTL came to a similar conclusion. In the Zlobinski et al study, they posit that these preferential pathways are due to the presence of non-uniform areas of hydrophobicity or hydrophilicity in the Ti PTL. Although they had no way to prove the statements, as neutron imaging is limited in their resolution. As our model electrolyzer used treated carbon paper, from our OCV image we do not observe significant hydrophobic locations, and the whole PTL is wetted. In addition, it should be noted that these findings are

comparable, as the porosity for the treated Freudenberg GDL is at 50 % compression is comparable, with a porosity of approximately <50 %.³⁰ These findings are novel, as this is the first time oxygen content has been directly observed and quantified on pore-scale in an operating PEM electrolyzer with x-ray computed tomography.

Since oxygen tends to take preferential pathways through the PTL, there are additive manufacturing strategies that can be used to take advantage of this tendency. One approach would be to machine microchannels, like the flow fields used to supply water to the MEA, in order to direct oxygen more efficiently through the PTL. Alternatively, another manufacturing strategy would be to pattern deliberate areas of higher hydrophobicity or hydrophilicity in the PTL in a process like photolithography to produce integrated circuits with the periodicity of 400 μm . By using these proposed manufacturing strategies, the removal of oxygen from the PEM electrolyzer would be more effective. In addition, studies on manufacturing PTLs with graded porosity found a significant decrease in mass transport limitations, and determined an optimal pore diameter to be between 6 and 11 μm , resulting in approximately 22% porosity³¹. This gradient of porosity could be engineered further to take advantage of the preferential pathway that oxygen takes as it exits the PTL.

References

1. Power-to-Gas Technology | SoCalGas. <https://www.socalgas.com/smart-energy/renewable-gas/power-to-gas>.
2. Sherif, S. A., Barbir, F. & Veziroglu, T. N. Wind energy and the hydrogen economy- review of the technology. *Sol. Energy* **78**, 647–660 (2005).
3. *Wind and Solar Curtailment*.
https://www.caiso.com/Documents/FlexibleResourcesHelpRenewables_FastFacts.pdf
(2020).
4. Buttler, A. & Spliethoff, H. Current status of water electrolysis for energy storage, grid balancing and sector coupling via power-to-gas and power-to-liquids: A review. *Renewable and Sustainable Energy Reviews* vol. 82 2440–2454 (2018).
5. Pascuzzi, S., Anifantis, A., Blanco, I. & Scarascia Mugnozza, G. Electrolyzer Performance Analysis of an Integrated Hydrogen Power System for Greenhouse Heating. A Case Study. *Sustainability* **8**, 629 (2016).
6. Mazloomi, K. & Gomes, C. Hydrogen as an energy carrier: Prospects and challenges. *Renew. Sustain. Energy Rev.* **16**, 3024–3033 (2012).
7. Züttel, A., Remhof, A., Borgschulte, A. & Friedrichs, O. Hydrogen: The future energy carrier. *Philosophical Transactions of the Royal Society A: Mathematical, Physical and Engineering Sciences* vol. 368 3329–3342 (2010).
8. Fuller, F. T. & Harb, J. N. 14. Industrial Electrolysis, Electrochemical Reactors, and Redox-Flow Batteries - Knovel. *John Wiley & Sons*
<https://app.knovel.com/web/view/khtml/show.v/rcid:kpEE000023/cid:kt011IBAH1/viewe>

- rType:khtml/root_slug:electrochemical-engineering/url_slug:industrial-electrolysis?&b-toc-cid=kpEE000023&b-toc-title=Electrochemical Engineering&b-toc-url-slug=introduction-b (2018).
9. Leonard, E. *et al.* Operando X-ray tomography and sub-second radiography for characterizing transport in polymer electrolyte membrane electrolyzer. *Electrochim. Acta* **276**, 424–433 (2018).
 10. Mitchell, T. M. *The Discipline of Machine Learning*. (2006).
 11. Webb, S. Deep learning for biology. *Nature* **554**, 555–557 (2018).
 12. Laurell, C., Sandström, C., Berthold, A. & Larsson, D. Exploring barriers to adoption of Virtual Reality through Social Media Analytics and Machine Learning – An assessment of technology, network, price and trialability. *J. Bus. Res.* **100**, 469–474 (2019).
 13. Anding, K., Haar, L., Polte, G., Walz, J. & Notni, G. Comparison of the performance of innovative deep learning and classical methods of machine learning to solve industrial recognition tasks. in *Photonics and Education in Measurement Science 2019* (eds. Zagar, B., Mazurek, P., Rosenberger, M. & Dittrich, P.-G.) vol. 11144 26 (SPIE, 2019).
 14. Babic, U., Suermann, M., Büchi, F. N., Gubler, L. & Schmidt, T. J. Critical Review—Identifying Critical Gaps for Polymer Electrolyte Water Electrolysis Development. *J. Electrochem. Soc.* **164**, F387–F399 (2017).
 15. Mayyas, A., Ruth, M., Pivovar, B., Bender, G. & Wipke, K. *Manufacturing Cost Analysis for Proton Exchange Membrane Water Electrolyzers*. <https://www.nrel.gov/docs/fy10osti/72740.pdf>. (2019).

16. Kang, Z. *et al.* Developing titanium micro/nano porous layers on planar thin/tunable LGDLs for high-efficiency hydrogen production. *Int. J. Hydrogen Energy* **43**, 14618–14628 (2018).
17. Seweryn, J., Biesdorf, J., Schmidt, T. J. & Boillat, P. Communication—Neutron Radiography of the Water/Gas Distribution in the Porous Layers of an Operating Electrolyser. *J. Electrochem. Soc.* **163**, F3009–F3011 (2016).
18. García-Valverde, R., Espinosa, N. & Urbina, A. Simple PEM water electrolyser model and experimental validation. in *International Journal of Hydrogen Energy* vol. 37 1927–1938 (Pergamon, 2012).
19. Abdin, Z., Webb, C. J. & Gray, E. M. Modelling and simulation of a proton exchange membrane (PEM) electrolyser cell. *Int. J. Hydrogen Energy* **40**, 13243–13257 (2015).
20. Han, B., Mo, J., Kang, Z. & Zhang, F. Y. Effects of membrane electrode assembly properties on two-phase transport and performance in proton exchange membrane electrolyzer cells. *Electrochim. Acta* **188**, 317–326 (2016).
21. Kang, Z. *et al.* Performance Modeling and Current Mapping of Proton Exchange Membrane Electrolyzer Cells with Novel Thin/Tunable Liquid/Gas Diffusion Layers. *Electrochim. Acta* **255**, 405–416 (2017).
22. Dedigama, I. *et al.* In situ diagnostic techniques for characterisation of polymer electrolyte membrane water electrolyzers - Flow visualisation and electrochemical impedance spectroscopy. *Int. J. Hydrogen Energy* **39**, 4468–4482 (2014).
23. Normile, S. J., Zenyuk, I. V, Hodes, M. & Panzer, M. *Novel X-Ray Imaging Techniques*

- for Ex-Situ and Operando Study of Polymer Electrolyte Fuel Cells.* (2018).
24. Pelt, D. M. *et al.* Integration of TomoPy and the ASTRA toolbox for advanced processing and reconstruction of tomographic synchrotron data. *J. Synchrotron Radiat.* **23**, 842–849 (2016).
 25. Frank, E., Hall, M. A., Witten, I. H. & Kaufmann, M. *WEKA Workbench Online Appendix for 'Data Mining: Practical Machine Learning Tools and Techniques'*. (2016).
 26. Leonard, E. *et al.* Interfacial analysis of a PEM electrolyzer using X-ray computed tomography. *Sustain. Energy Fuels* 921–931 (2020) doi:10.1039/c9se00364a.
 27. Maier, M. *et al.* Mass transport in polymer electrolyte membrane water electrolyser liquid-gas diffusion layers: A combined neutron imaging and X-ray computed tomography study. *J. Power Sources* **455**, 227968 (2020).
 28. Mateusz, Z. Transient and Steady State Two-Phase Flow in Anodic Porous Transport Layer of Proton Exchange Membrane Water Electrolyzer. (2020) doi:10.1149/1945-7111/ab8c89.
 29. Zenyuk, I. V., Parkinson, D. Y., Connolly, L. G. & Weber, A. Z. Gas-diffusion-layer structural properties under compression via X-ray tomography. *J. Power Sources* **328**, 364–376 (2016).
 30. Lettenmeier, P. *et al.* Comprehensive investigation of novel pore-graded gas diffusion layers for high-performance and cost-effective proton exchange membrane electrolyzers. *Energy Environ. Sci.* **10**, 2521–2533 (2017).